IEEE Access
Multidisciplinary | Rapid Review | Open Access Journal

Received January 25, 2019, accepted February 19, 2019, date of publication March 13, 2019, date of current version March 26, 2019.

Digital Object Identifier 10.1109/ACCESS.2019.2901805

A 3D Wideband Non-Stationary Multi-Mobility Model for Vehicle-to-Vehicle MIMO Channels

JI BIAN[1], CHENG-XIANG WANG[2], (Fellow, IEEE), JIE HUANG[2], YU LIU[1], JIAN SUN[1], (Member, IEEE), MINGGAO ZHANG[1], AND EL-HADI M. AGGOUNE[3], (Senior Member, IEEE)

[1]Shandong Provincial Key Lab of Wireless Communication Technologies, School of Information Science and Engineering, Shandong University, Qingdao 266237, China
[2]National Mobile Communications Research Laboratory, School of Information Science and Engineering, Southeast University, Nanjing 210096, China
[3]Sensor Networks and Cellular Systems Research Center, University of Tabuk, Tabuk 47315/4031, Saudi Arabia

Corresponding author: Cheng-Xiang Wang (chxwang@seu.edu.cn)

This work was supported in part by the Natural Science Foundation of China under Grant 61771293, in part by the Fundamental Research Funds for the Central Universities, in part by SNCS, University of Tabuk, under Grant S-1439-0163, in part by the Science and Technology Project of Guangzhou under Grant 201704030105, in part by the EU H2020 Research and Innovation Staff Exchanges TESTBED Project under Grant 734325, in part by the Key R&D Program of Shandong Province under Grant 2016GGX101014, in part by the Fundamental Research Funds of Shandong University under Grant 2017JC029, in part by the Taishan Scholar Program of Shandong Province, in part by the National Postdoctoral Program for Innovative Talents under Grant BX201700308 and Grant BX20180062, and in part by the China Postdoctoral Science Foundation Funded Project under Grant 2017M622203.

ABSTRACT In this paper, a three-dimensional non-stationary multi-mobility vehicle-to-vehicle channel model is proposed. The channel model considers a realistic propagation environment where the transmitter (Tx), receiver (Rx), and scatterers can experience changes in their speeds and moving directions. With different trajectories of the Tx and Rx, the impacts of antenna array rotation are incorporated. The channel impulse response of the proposed multi-mobility channel model is derived using time-varying channel parameters such as angles, delays, and powers. Besides, a simplified two-dimensional non-stationary multi-mobility channel model with approximate expressions is provided. Key statistical properties, e.g., local spatial-temporal cross-correlation function and stationary interval are derived and investigated. The usefulness of the proposed model is validated by comparing the local Doppler power spectrum density and local Doppler spread with the corresponding measurement data. The presented results indicate that the speed and trajectory variations of the Tx and Rx, as well as the motion of scatterers, can have major impacts on channel statistical properties and intensify the channel non-stationarity.

INDEX TERMS Non-stationary V2V MIMO channels, GBSM, scatterer motion, trajectory and velocity variations, statistical properties.

I. INTRODUCTION

The revolutionary communication technologies employed in the fifth generation (5G) communication systems put higher requirements for 5G channel modeling [1]–[3]. The biggest challenge in the research area of wireless channel modeling is to develop efficient and accurate channel models which can mimic all the propagation characteristics affecting the performance analysis of wireless communication systems. The vehicle-to-vehicle (V2V) channel modeling, as one of the hottest topics in 5G channel modeling, has drawn increasing attention from researchers [4], [5]. In V2V communication scenarios, both the transmitter (Tx) and receiver (Rx) are surrounded by a great number of scatterers. The Tx, Rx, and scatterers, e.g. passing vehicles, can be moving, which result in fast-changing propagation environments. The multi-mobility characteristics make V2V channels distinctly different from conventional cellular channels and can significantly increase the channel model complexity [6]–[8].

Channel measurements show that V2V channels illustrate non-stationary properties resulting from the high speeds of the Tx and Rx and the fast-changing environments [9], [10]. However, most existing V2V channel models in the literature were developed based on the wide-sense stationary (WSS) assumption. In [11] and [12], two-dimensional (2D) regular-shaped geometry-based stochastic models (RS-GBSMs) for V2V channels were developed. The model is a combination of a two-ring model and an ellipse model, which makes the

The associate editor coordinating the review of this manuscript and approving it for publication was Franco Fuschini.

model more generic and can be adapted to different V2V scenarios. Three-dimensional (3D) RS-GBSMs for V2V channels with verification by the measurement data were proposed in [13] and [14]. The models were developed by assuming scatterers located on the surfaces of multiple cylinders centered at the Tx and Rx. By extending the 2D channel model in [11] into 3D, a more realistic V2V channel model was presented in [15]. The angles of waves in the 3D space were modeled by the von Mises Fisher (VMF) distribution. However, the above-mentioned models [11]–[15] cannot capture the non-stationary characteristics of the channels, which can result in erroneous evaluation of system performance [16].

For the non-stationary V2V channel modeling, most researchers focus on characterizing the dynamic behaviors of clusters, which can be resulted from the moving scatterers, e.g., pedestrians and vehicles [17]. In [18] and [19], 2D V2V channel models were proposed by considering fixed and moving scatterers in propagation environments. The movement of scatterers results in time-varying angles of arrival (AoAs) and angles of departure (AoDs), which were calculated based on the geometrical relationship. However, the Tx, Rx, and scatterers were only allowed to move with constant speeds in given directions. A 3D non-stationary V2V channel model was presented in [20], which was the extension of the stationary channel model in [15]. The model combined a two-sphere model and a multiple confocal elliptic-cylinder model, accounting for moving vehicles and stationary roadside environments, respectively. However, only constant speeds and moving directions were allowed. Besides, the scatterers around the Tx(Rx) were assumed to move with the same speed and moving direction of the Tx(Rx), which results in time-invariant AoAs and AoDs, and may be contrary to realistic environments. Borhani and Pätzold [21] proposed a single-input single-output (SISO) V2V channel model where the speeds and moving directions of scatterers were described using certain distributions, e.g., uniform and Gaussian mixture distributions. However, all the channel parameters such as angles, powers, as well as the speeds and moving directions of the mobile stations (MSs) and scatterers are time-invariant, which makes the model not be able to sufficiently characterize the non-stationarity of V2V channels. Besides, only single-bounced components were considered.

In real-world environments, the Tx, Rx, and scatterers can experience changes in their speeds and moving directions. However, most existing V2V channel models were developed based on the constant velocity assumption, i.e., Tx/Rx travels with a constant speed along a straight line [11]–[15], [17]–[24]. Few channel models consider the speed and/or trajectory variations of the Tx/Rx and the effects of velocity variations on channel statistics are widely unknown. In [25], the fixed-to-mobile (F2M) channels were modeled using a sum-of-chirps (SOC_h) process, which was extended from the well-known sum-of-cisoids (SOC_i) process by considering the time-varying speed of the MS. The time and frequency properties of the SOC_h process were derived and analyzed. Following the similar approach, a V2V channel model considering the velocity variations of the Tx and Rx can be found in [26]. Based on the vector method, a time-frequency dispersive V2V channel model considering the speed variations of the Tx and Rx was proposed in [27]. The temporal and frequency correlations of the model were studied. However, in [25] and [26], only the velocities of the MS changed over time. Channel parameters such as angles and powers are time-invariant. Channel models in [25] and [27] only considered single-bounced components and neglected the multi-bounced components, which can cause incorrect statistics of V2V channels [11]. Besides, channel models in [25]–[27] are 2D SISO channel models. Therefore, they cannot reflect the impacts of antenna array rotation on the channel characteristics when the MS travels along certain trajectories. The scatterers of those models were assumed to be fixed, without considering their mobility. A 3D F2M non-stationary channel model can be found in [28], where the WINNER+ channel model was extended by relaxing the constant velocity assumption. The time variations of channel parameters and scatterer movements were considered. Recently, a 2D non-stationary V2V channel model was proposed by combining a two-ring model and a Gauss-Markov mobility model [29]. The model aims to capture the impacts of random trajectories of the MS on channel characteristics. However, the scatterers of the model were fixed and time variations of the channel parameters were not considered. Besides, in [28] and [29], the path phases were calculated by simply substituting the time-invariant Doppler frequencies with time-varying Doppler frequencies. The calculation method of path phases stemmed from that in stationary case, which makes the calculation of path phases not sufficiently accurate and may lead to erroneous results in system evaluation [30].

To the best of the authors' knowledge, a 3D non-stationary multiple-input multiple-output (MIMO) V2V channel model allowing for time-varying speeds and arbitrary trajectories of the Tx, Rx, and scatterers and incorporating the effects of antenna array rotations is still missing in the literature. The statistical properties such as temporal autocorrelation function (ACF), spatial cross-correlation function (CCF), and non-stationarity of such a channel model have not been thoroughly researched. This paper aims to fill these gaps. The major contributions of this paper are summarized as follows:

1) A 3D wideband non-stationary multi-mobility MIMO channel model is developed with time-varying channel parameters. The speeds and trajectories of the Tx, Rx, and scatterers are allowed to change. The impacts of arbitrary rotation of antenna array are incorporated. The proposed model can include many existing channel models as special cases or reduce to simple channel models by adjusting channel model parameters properly.
2) A highly-efficient 2D non-stationary multi-mobility channel model is proposed. The temporal ACF and spatial CCF of the model are investigated with closed-from expressions.

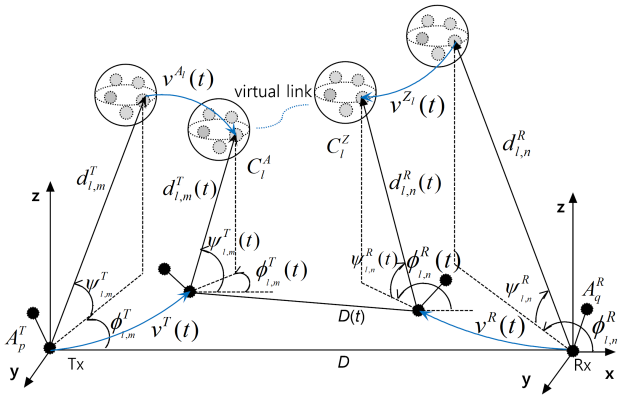

FIGURE 1. The non-stationary multi-mobility MIMO channel model with time-varying velocities of the Tx, Rx, and scatterers.

3) Statistical properties including temporal ACF, spatial CCF, and stationary interval are verified by comparing the theoretical results with the corresponding simulated and approximated results. The impacts of speed and trajectory variations of the Tx/Rx and the motion of scatterers on statistical properties are analyzed.
4) The proposed mode is validated by the corresponding measurement data in terms of local Doppler power spectrum density (PSD) and local Doppler spread.

The remainder of this paper is organized as follows. In Section II, the proposed non-stationary multi-mobility channel model is introduced, including the geometric construction and the channel impulse response (CIR). Statistics of the proposed channel model are derived and investigated in Section III. In Section IV, numerical and simulation results are illustrated and discussed. Conclusions are finally given in Section V.

II. THE 3D NON-STATIONARY MULTI-MOBILITY CHANNEL MODEL

The geometrical description of the 3D non-stationary multi-mobility MIMO channel model is illustrated in Fig. 1. For the sake of clarity, only the l-th ($l = 1, \ldots, L$) path is shown in this figure. At the initial time t_0, the Tx and the Rx are located on the x axis with a distance of D. Both the Tx and Rx are equipped with arbitrary-shaped antenna arrays, such as uniform linear arrays and rectangular arrays. The initial positions of the p-th ($p = 1, \ldots, M_T$) Tx antenna element A_p^T and the q-th ($q = 1, \ldots, M_R$) Rx antenna element A_q^R are described by location vectors $\mathbf{r}_p^T$ and $\mathbf{r}_q^R$, respectively. Note that both $\mathbf{r}_p^T = [r_{p,x}^T, r_{p,y}^T, r_{p,z}^T]^{\mathrm{T}}$ and $\mathbf{r}_q^R = [r_{q,x}^R, r_{q,y}^R, r_{q,z}^R]^{\mathrm{T}}$ are in the local coordinate systems with their origins at A_1^T and A_1^R, respectively. The propagations from the Tx to Rx can be divided into the first bounce propagation via the cluster C_l^A, the last bounce propagation via the cluster C_l^Z, and the propagation between C_l^A and C_l^Z, which is abstracted as the virtual link [31]. The azimuth AoDs (AAoDs) and elevation AoDs (EAoDs) of the m-th ray in the l-th cluster are denoted by $\phi_{l,m}^T$ and $\psi_{l,m}^T$, respectively. Similarly, $\phi_{l,n}^R$ and $\psi_{l,n}^R$ account for the azimuth AoAs (AAoAs) and elevation AoAs (EAoAs) of the n-th ray in the l-th cluster, respectively. The travel distance between the Tx and C_l^A via the m-th ($m = 1, \ldots, M_l$) ray is denoted by $d_{l,m}^T$. Symbol $d_{l,n}^R$ is the travel distance between the Rx and C_l^Z via the n-th ($n = 1, \ldots, N_l$) ray. Note that the angles $\phi_{l,m}^T$, $\psi_{l,m}^T$, $\phi_{l,n}^R$, and $\psi_{l,n}^R$ and distances D, $d_{l,m}^T$, and $d_{l,n}^R$ are captured at the initial time instant t_0. The time evolution of the model will be introduced in the rest of this section. In the proposed model, the Tx, Rx, and clusters, i.e., C_l^A, and C_l^Z, are allowed to move with time-varying speeds and arbitrary trajectories, which are described by the velocity vector $\mathbf{v}^X(t)$ with speed $v^X(t)$, travel elevation angle $\alpha_E^X(t)$, and travel azimuth angle $\alpha_A^X(t)$, where $X = \{T, R, A_l, Z_l\}$. The AAoD and EAoD of the line-of-sight (LoS) path at initial time instant are denoted by ϕ_{LoS}^T and ψ_{LoS}^T, respectively. Similarly, ϕ_{LoS}^R and ψ_{LoS}^R account for the AAoA and EAoA of the LoS path at initial time instant, respectively. The definitions of key parameters of the proposed channel model are listed in Table 1.

A. CHANNEL IMPULSE RESPONSE

Considering the MIMO channel matrix $\mathbf{H}(t) = [h_{qp}(t)]_{M_R \times M_T}$, the CIR between A_p^T and A_q^R can be calculated as a summation of the LoS component and non-line-of-sight (NLoS) components, and is expressed as [15]

$$h_{qp}(t,\tau) = \sqrt{\frac{K}{K+1}} h_{qp}^{\mathrm{LoS}}(t)\delta(\tau - \tau^{\mathrm{LoS}}(t)) + \sqrt{\frac{1}{K+1}} \sum_{l=1}^{L} h_{qp,l}(t)\delta(\tau - \tau_l(t)) \quad (1)$$

where K is the Ricean factor, $\delta(\cdot)$ is the Dirac delta function, $\tau^{\mathrm{LoS}}(t)$ and $\tau_l(t)$ are the time-varying delays of the LoS path and the l-th cluster, repectively.

1) FOR THE NLoS COMPONENTS

The channel coefficients between A_p^T and A_q^R via the l-th cluster consisting $M_l \cdot N_l$ rays can be expressed as [32]

$$\begin{aligned} h_{qp,l}(t) &= \Pi_{T_0}(t) \lim_{M_l, N_l \to \infty} \sqrt{\frac{P_l(t)}{M_l N_l}} \sum_{m,n=1}^{M_l N_l} \begin{bmatrix} F_{q,V}(\psi_{l,n}^R, \phi_{l,n}^R) \\ F_{q,H}(\psi_{l,n}^R, \phi_{l,n}^R) \end{bmatrix}^{\mathrm{T}} \\ &\times \begin{bmatrix} e^{j\vartheta_{l,mn}^{VV}} & \sqrt{\kappa_{l,mn}^{-1}} e^{j\vartheta_{l,mn}^{VH}} \\ \sqrt{\kappa_{l,mn}^{-1}} e^{j\vartheta_{l,mn}^{HV}} & e^{j\vartheta_{l,mn}^{HH}} \end{bmatrix} \begin{bmatrix} F_{p,V}(\psi_{l,m}^T, \phi_{l,m}^T) \\ F_{p,H}(\psi_{l,m}^T, \phi_{l,m}^T) \end{bmatrix} \\ &\times \exp\{j[\theta_{l,mn}(t) + \varphi_{qp,l,mn}(t)]\} \end{aligned} \quad (2)$$

where $\{\cdot\}^{\mathrm{T}}$ stands for transposition, $F_{p(q),V}$ and $F_{p(q),H}$ are the radiation patterns of $A_p^T(A_q^R)$ for vertical and horizontal polarizations, respectively, $\kappa_{l,mn}$ is the cross polarization power ratio, $\vartheta_{l,mn}^{VV}$, $\vartheta_{l,mn}^{VH}$, $\vartheta_{l,mn}^{HV}$, and $\vartheta_{l,mn}^{HH}$ are initial phases for four different polarization combinations and modeled as random variables uniformly distributed over $(0, 2\pi]$. $\Pi_{T_0}(t)$

TABLE 1. Summary of key parameter definitions.

C_l^A, C_l^Z	the first and last bounce clusters of the l-th path, respectively
A_p^T, A_q^R	the p-th Tx antenna element and the q-th Rx antenna element, respectively
$\mathbf{r}_p^T$, $\mathbf{r}_q^R$	3D location vectors of A_p^T and A_q^R at t_0, respectively
$d_{l,m}^T$	distances between the Tx and C_l^A via the m-th ray at t_0
$d_{l,n}^R$	distances between the Rx and C_l^Z via the n-th ray at t_0
D	distance between the Tx and Rx at t_0
$\mathbf{v}^X(t)$	velocity vectors of the Tx, Rx, C_l^A, and C_l^Z, $X = \{T, R, A_l, Z_l\}$
$\alpha_E^X(t)$	travel elevation angle of the Tx, Rx, C_l^A, and C_l^Z, $X = \{T, R, A_l, Z_l\}$
$\alpha_A^X(t)$	travel azimuth angle of the Tx, Rx, C_l^A, and C_l^Z, $X = \{T, R, A_l, Z_l\}$
$v^X(t)$	speeds of the Tx, Rx, C_l^A, and C_l^Z, $X = \{T, R, A_l, Z_l\}$
$\phi_{l,m}^T$, $\psi_{l,m}^T$	AAoD and EAoD of the m-th ray in the l-th cluster at t_0, respectively
$\phi_{l,n}^R$, $\psi_{l,n}^R$	AAoA and EAoA of the n-th ray in the l-th cluster at t_0, respectively
ϕ_{LoS}^T, ψ_{LoS}^T	AAoD and EAoD of the LoS path at t_0, respectively
ϕ_{LoS}^R, ψ_{LoS}^R	AAoA and EAoA of the LoS path at t_0, respectively

is the rectangular window function, and is defined as [27]

$$\Pi_{T_0}(t) = \begin{cases} 1, & 0 \leqslant t \leqslant T_0 \\ 0, & \text{otherwise.} \end{cases} \tag{3}$$

Here, T_0 is the observation time interval. In (2), $P_l(t)$ is the time-varying power of the l-th path. The total Doppler frequencies of the proposed model can be considered as the result of two effects, i.e., the movements of the Tx, Rx, and scatterers, and the antenna array rotations on both sides. Considering the time-varying velocities, the phase shifts $\theta_{l,mn}(t)$ caused by the movements of the Tx, Rx, and scatterers should be calculated as [33]

$$\begin{aligned}\theta_{l,mn}(t) &= \theta_{l,m}^{T/A_l}(t) + \theta_{l,n}^{R/Z_l}(t) \\ &= 2\pi\left(\int_0^t f_{l,m}^{T/A_l}(t)\mathrm{d}t + \int_0^t f_{l,n}^{R/Z_l}(t)\mathrm{d}t\right) + \theta_{l,mn}(0)\end{aligned} \tag{4}$$

where $\theta_{l,mn}(0)$ are the initial phase shifts and modeled as random variable uniformly distributed over $(0, 2\pi]$. The time-varying Doppler frequencies resulting from the movements of the Tx, Rx, and scatterers can be expressed as

$$f_{l,m}^{T/A}(t) = \left\langle \mathbf{v}^T(t) - \mathbf{v}^{A_l}(t),\, \Phi_{l,m}^T(t) \right\rangle / \lambda \tag{5}$$

$$f_{l,n}^{R/Z}(t) = \left\langle \mathbf{v}^R(t) - \mathbf{v}^{Z_l}(t),\, \Phi_{l,n}^R(t) \right\rangle / \lambda \tag{6}$$

respectively, where $\langle\cdot\rangle$ denotes inner product, λ stands for the wavelength. The time-varying velocity vector $\mathbf{v}^X(t)$ is given by

$$\mathbf{v}^X(t) = v^X(t) \begin{bmatrix} \cos(\alpha_E^X(t))\cos(\alpha_A^X(t)) \\ \cos(\alpha_E^X(t))\sin(\alpha_A^X(t)) \\ \sin(\alpha_E^X(t)) \end{bmatrix}^{\mathrm{T}} \tag{7}$$

where $X = \{T, R, A_l, Z_l\}$. For clarity, Fig. 2 shows the projection of the non-stationary multi-mobility channel model.

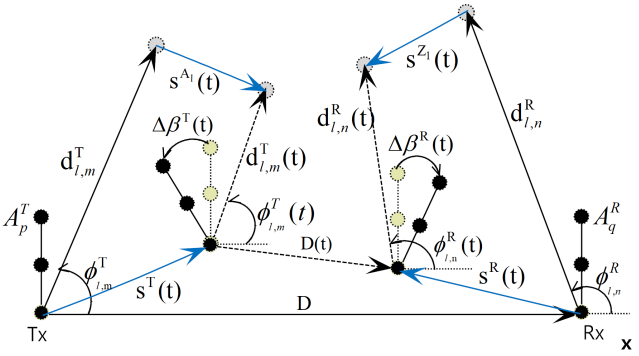

FIGURE 2. The projection of the non-stationary multi-mobility MIMO channel model.

The time-varying departure angle unit vector $\Phi_{l,m}^T$ and arrival angle unite vector $\Phi_{l,n}^R$ can be determined as

$$\Phi_{l,m}^T(t) = \frac{\mathbf{d}_{l,m}^T(t)}{\left\|\mathbf{d}_{l,m}^T(t)\right\|} = \frac{\mathbf{d}_{l,m}^T + \mathbf{s}^{A_l}(t) - \mathbf{s}^T(t)}{\left\|\mathbf{d}_{l,m}^T + \mathbf{s}^{A_l}(t) - \mathbf{s}^T(t)\right\|} \tag{8}$$

$$\Phi_{l,n}^R(t) = \frac{\mathbf{d}_{l,n}^R(t)}{\left\|\mathbf{d}_{l,n}^R(t)\right\|} = \frac{\mathbf{d}_{l,n}^R + \mathbf{s}^{Z_l}(t) - \mathbf{s}^R(t)}{\left\|\mathbf{d}_{l,n}^R + \mathbf{s}^{Z_l}(t) - \mathbf{s}^R(t)\right\|} \tag{9}$$

where $\|\cdot\|$ stands for the Euclidean norm, $\mathbf{s}^X(t) = \int_0^t \mathbf{v}^X(t)\mathrm{d}t$, are the displacement vectors of the Tx, Rx, C_l^A, and C_l^Z during time interval $[0, t]$. Position vectors $\mathbf{d}_{l,m}^T$ from the Tx to C_l^A and $\mathbf{d}_{l,n}^R$ from the Rx to C_l^Z can be expressed as

$$\begin{aligned}\mathbf{d}_{l,m}^T &= d_{l,m}^T \cdot \begin{bmatrix} \cos(\psi_{l,m}^T)\cos(\phi_{l,m}^T) \\ \cos(\psi_{l,m}^T)\sin(\phi_{l,m}^T) \\ \sin(\psi_{l,m}^T) \end{bmatrix}^{\mathrm{T}} \\ \mathbf{d}_{l,n}^R &= d_{l,n}^R \cdot \begin{bmatrix} \cos(\psi_{l,n}^R)\cos(\phi_{l,n}^R) \\ \cos(\psi_{l,n}^R)\sin(\phi_{l,n}^R) \\ \sin(\psi_{l,n}^R) \end{bmatrix}^{\mathrm{T}}.\end{aligned} \tag{10}$$

Note that the phase calculation in (4) is different from those in [17]–[20] and [29], where the calculation method was taken from the stationary case, i.e., simply replacing the time-invariant Doppler frequencies by time-varying Doppler frequencies. This method results in the incorrect relationship between phase and Doppler frequency [33], and therefore not suitable for non-stationary channel models.

In (2), $\varphi_{qp,l,mn}(t)$ are the phase shifts associated with the antenna array rotations on both sides, and can be further expressed as

$$\varphi_{qp,l,mn}(t) = \varphi^T_{p,l,m}(t) + \varphi^R_{q,l,n}(t) \tag{11}$$

where

$$\varphi^T_{p,l,m}(t) = k_0 \left\langle (\mathbf{M}^T(t)\mathbf{r}^T_p)^{\mathrm{T}}, \Phi^T_{l,m}(t) \right\rangle \tag{12}$$

$$\varphi^R_{q,l,n}(t) = k_0 \left\langle (\mathbf{M}^R(t)\mathbf{r}^R_q)^{\mathrm{T}}, \Phi^R_{l,n}(t) \right\rangle. \tag{13}$$

Here, $k_0 = 2\pi/\lambda$ is the wavenumber. The arrays on both sides can rotate with arbitrary trajectories of the Tx and Rx. The rotation matrices $\mathbf{M}^T(t)$ and $\mathbf{M}^R(t)$ are introduced in order to obtain the 3D coordinates of the A^T_p and A^R_q at time instant t, respectively. The rotation matrices on the Tx and Rx can be expressed as

$$\mathbf{M}^X(t) = \begin{bmatrix} \cos\left(\Delta\beta^X_A(t)\right) & -\sin\left(\Delta\beta^X_A(t)\right) & 0 \\ \sin\left(\Delta\beta^X_A(t)\right) & \cos\left(\Delta\beta^X_A(t)\right) & 0 \\ 0 & 0 & 1 \end{bmatrix} \times \begin{bmatrix} \cos\left(\Delta\beta^X_E(t)\right) & 0 & -\sin\left(\Delta\beta^X_E(t)\right) \\ 0 & 1 & 0 \\ \sin\left(\Delta\beta^X_E(t)\right) & 0 & \cos\left(\Delta\beta^X_E(t)\right) \end{bmatrix} \tag{14}$$

where $X = \{T, R\}$, $\Delta\beta^X_A(t) = \beta^X_A(t) - \beta^X_A$ and $\Delta\beta^X_E(t) = \beta^X_E(t) - \beta^X_E$ are the azimuth and elevation rotation angles of the Tx/Rx array relative to the initial positions, respectively, $\beta^X_E(t)$ and $\beta^X_A(t)$ are the elevation and azimuth angles of the Tx/Rx array at time t. In (1), the time-varying delay of the l-th path, i.e., $\tau_l(t)$ can be obtained as

$$\tau_l(t) = \frac{d^T_l(t) + d^R_l(t)}{c_0} + \tilde{\tau}_l \tag{15}$$

where c_0 is the speed of light, $d^T_l(t) = \mathbb{E}\{\|\mathbf{d}^T_{l,m}(t)\|\}$, $d^R_l(t) = \mathbb{E}\{\|\mathbf{d}^R_{l,n}(t)\|\}$, $\tilde{\tau}_l$ is the delay of the virtual link between C^A_l and C^Z_l, and is determined as $\tilde{\tau}_l = \tilde{d}_l/c_0 + \tilde{\tau}_{l,\mathrm{link}}$, $\tilde{d}_l$ is the distance between C^A_l and C^Z_l, $\tilde{\tau}_{l,\mathrm{link}}$ is a nonnegative random variable following exponential distribution [34]. When $\tilde{\tau}_l = 0$, i.e., $\tilde{d}_l = 0$ and $\tilde{\tau}_{l,\mathrm{link}} = 0$, multi-bounced propagations reduce to single-bounced propagations.

Channel measurements show that in most scenarios, the power of clusters can be modeled by exponential power delay profile [31], [35]. Using the time-varying delays, the time-varying cluster powers can be determined as

$$P'_l(t) = \exp\{-\tau_l(t) \cdot \frac{r_\tau - 1}{r_\tau \sigma_\tau}\} \cdot 10^{\frac{-Z_l}{10}} \tag{16}$$

where r_τ stands for the delay distribution proportionality factor, σ_τ accounts for the delay spread, Z_l is the per cluster shadowing term in dB. Finally, the cluster powers are normalized as

$$P_l(t) = \frac{P'_l(t)}{\sum_{l=1}^{L} P'_l(t)}. \tag{17}$$

2) FOR THE LOS COMPONENT

The complex channel gain $h^{\mathrm{LoS}}_{qp}(t)$ is given by

$$\begin{aligned} h^{\mathrm{LoS}}_{qp}(t) &= \Pi_{T_0}(t) \begin{bmatrix} F_{q,V}(\psi^R_{\mathrm{LoS}}, \phi^R_{\mathrm{LoS}}) \\ F_{q,H}(\psi^R_{\mathrm{LoS}}, \phi^R_{\mathrm{LoS}}) \end{bmatrix}^{\mathrm{T}} \begin{bmatrix} e^{j\vartheta^{VV}_{\mathrm{LoS}}} & 0 \\ 0 & e^{j\vartheta^{HH}_{\mathrm{LoS}}} \end{bmatrix} \\ &\times \begin{bmatrix} F_{p,V}(\psi^T_{\mathrm{LoS}}, \phi^T_{\mathrm{LoS}}) \\ F_{p,H}(\psi^T_{\mathrm{LoS}}, \phi^T_{\mathrm{LoS}}) \end{bmatrix} \exp\{j[\theta_{\mathrm{LoS}}(t) + \varphi_{pq,\mathrm{LoS}}(t)]\}. \end{aligned} \tag{18}$$

where $\vartheta^{VV}_{\mathrm{LoS}}$ and $\vartheta^{HH}_{\mathrm{LoS}}$ are initial phases of the LoS path for polarization combinations $\{VV, HH\}$ and uniformly distributed within $(0, 2\pi]$. The phase shifts caused by the movements of the Tx and Rx are obtained as

$$\theta_{\mathrm{LoS}}(t) = k_0 \int_0^t \left\langle \mathbf{v}^R(t) - \mathbf{v}^T(t), \Phi^R_{\mathrm{LoS}}(t) \right\rangle \mathrm{d}t \tag{19}$$

where $\Phi^T_{\mathrm{LoS}}(t)$ is the departure angle unit vector of the LoS path, and can be obtained as

$$\Phi^T_{\mathrm{LoS}}(t) = \frac{\mathbf{D}(t)}{\|\mathbf{D}(t)\|} = \frac{\mathbf{D} + \mathbf{s}^R(t) - \mathbf{s}^T(t)}{\left\|\mathbf{D} + \mathbf{s}^R(t) - \mathbf{s}^T(t)\right\|}. \tag{20}$$

Here, $\mathbf{D} = [D, 0, 0]$ is the position vector from the Tx to Rx at initial time instant. The phase shifts due to the antenna array rotations on both link ends, i.e., $\varphi_{pq,\mathrm{LoS}}(t) = \varphi^T_{p,\mathrm{LoS}}(t) + \varphi^R_{q,\mathrm{LoS}}(t)$, can be expressed as

$$\varphi^T_{p,\mathrm{LoS}}(t) = k_0 \left\langle (\mathbf{M}^T(t)\mathbf{r}^T_p)^{\mathrm{T}}, \Phi^T_{\mathrm{LoS}}(t) \right\rangle \tag{21}$$

$$\varphi^R_{q,\mathrm{LoS}}(t) = -k_0 \left\langle (\mathbf{M}^R(t)\mathbf{r}^R_q)^{\mathrm{T}}, \Phi^T_{\mathrm{LoS}}(t) \right\rangle. \tag{22}$$

Therefore, the time-varying delay of the LoS path is determined as $\tau^{\mathrm{LoS}}(t) = \|\mathbf{D}(t)\|/c_0$.

It is worth noting that the proposed model has been developed based on multi-bounced scattering concept. For simplicity, the first bounce and last bounce propagation paths were assumed to be independent, as in the WINNER II channel model [32]. For the scenarios where the scatterers around the Tx and Rx are closely located, the dependence between the two link ends can exist. Channel models using the independence assumption may result in erroneous results in system evaluation [36]. For example, it forces the joint direction of departure-direction of arrival (DoD-DoA) spectrum to be represented as the product of DoD and DoA spectrums, which can make the model underestimates the mutual information and overestimate the channel diversity [37].

B. APPROXIMATE EXPRESSIONS OF 2D NON-STATIONARY MULTI-MOBILITY CHANNEL MODEL

For the scenarios where the distances between the Tx/Rx and scatterers are far enough, such as rural macro-cell (RMa) and suburban macro-cell (SMa), a 2D channel model can

exhibit satisfactory performance. In this subsection, a highly-efficient 2D non-stationary multi-mobility channel model with approximate expressions is developed. Considering a typical V2V communication scenario, where the Tx and Rx are surrounded by scatterers, such as vehicles and pedestrians. The Tx, Rx, and scatterers can move in the horizontal plane with their speeds and travel angles vary linearly during the time interval T_0, i.e., $v^X(t) = v_0^X + a^X \cdot t$ and $\alpha^X(t) = \alpha_0^X + \omega^X \cdot t$ where v_0^X, a^X, α_0^X, and ω^X are the initial speeds, accelerations, initial travel angles, and angular speeds of the the Tx, Rx, C_l^A, and C_l^Z, respectively, where $X = \{T, R, A_l, Z_l\}$.

1) FOR THE NLoS COMPONENTS

The channel coefficients of the NLoS components can refer to (2). By imposing the elevation angles in (8) and (9) into zero, the time-varying AAoDs $\phi_{l,m}^T(t)$ and AAoAs $\phi_{l,n}^R(t)$ can be obtained as

$$\begin{aligned}\phi_{l,m}^T(t) = \mathrm{Arg}\{&d_{l,m}^T\cos(\phi_{l,m}^T) + \int_0^t v^{A_l}(t)\cos(\alpha^{A_l}(t))\mathrm{d}t \\ &- \int_0^t v^T(t)\cos(\alpha^T(t))\mathrm{d}t, \\ &\times d_{l,m}^T\sin(\phi_{l,m}^T) + \int_0^t v^{A_l}(t)\sin(\alpha^{A_l}(t))\mathrm{d}t \\ &- \int_0^t v^T(t)\sin(\alpha^T(t))\mathrm{d}t\}\end{aligned} \tag{23}$$

$$\begin{aligned}\phi_{l,n}^R(t) = \mathrm{Arg}\{&d_{l,n}^R\cos(\phi_{l,n}^R) + \int_0^t v^{Z_l}(t)\cos(\alpha^{Z_l}(t))\mathrm{d}t \\ &- \int_0^t v^R(t)\cos(\alpha^R(t))\mathrm{d}t, \\ &\times d_{l,n}^R\sin(\phi_{l,n}^R) + \int_0^t v^{Z_l}(t)\sin(\alpha^{Z_l}(t))\mathrm{d}t \\ &- \int_0^t v^R(t)\sin(\alpha^R(t))\mathrm{d}t\}\end{aligned} \tag{24}$$

where Arg{·} returns the angle of a 2D vector. According to the method in [38], the time-varying angles $\phi_{l,m}^T(t)$ and $\phi_{l,n}^R(t)$ can be approximated as

$$\phi_{l,m}^T(t) \approx \phi_{l,m}^T + \gamma_{l,m}^T \cdot t \tag{25}$$

$$\phi_{l,n}^R(t) \approx \phi_{l,n}^R + \gamma_{l,n}^R \cdot t \tag{26}$$

where

$$\gamma_{l,m}^T = [v_0^{A_l}\sin(\alpha_0^{A_l} - \phi_{l,m}^T) + v_0^T\sin(\phi_{l,m}^T - \alpha_0^T)]/d_{l,m}^T \tag{27}$$

$$\gamma_{l,n}^R = [v_0^{Z_l}\sin(\alpha_0^{Z_l} - \phi_{l,n}^R) + v_0^R\sin(\phi_{l,n}^R - \alpha_0^R)]/d_{l,n}^R. \tag{28}$$

The approximations can achieve satisfactory accuracy when the observation time interval is small, e.g., several seconds. Therefore, the time-varying Doppler frequencies resulting from the relative movement between the Tx/Rx and scatterers in (5) and (6) can be rewritten as

$$f_{l,m}^{T/A_l}(t) = f_{l,m}^T(t) - f_{l,m}^{A_l}(t) \tag{29}$$

$$f_{l,n}^{R/Z_l}(t) = f_{l,n}^R(t) - f_{l,n}^{Z_l}(t) \tag{30}$$

where

$$f_{l,m}^{T(A_l)}(t) = \frac{v^{T(A_l)}(t)}{\lambda}\cos[\phi_{l,m}^T(t) - \alpha^{T(A_l)}(t)] \tag{31}$$

$$f_{l,n}^{R(Z_l)}(t) = \frac{v^{R(Z_l)}(t)}{\lambda}\cos[\phi_{l,n}^R(t) - \alpha^{R(Z_l)}(t)]. \tag{32}$$

By substituting (31) and (32) into (4), the phase changes $\theta_{l,mn}(t)$ can be calculated as

$$\theta_{l,mn}(t) = \theta_{l,m}^T(t) - \theta_{l,m}^{A_l}(t) + \theta_{l,n}^R(t) - \theta_{l,n}^{Z_l}(t) + \theta_{l,mn}(0) \tag{33}$$

where

$$\begin{aligned}&\theta_{l,m}^{T(A)}(t) \\ &= k_0(\gamma_{l,m}^T - \omega^{T(A)})^{-2}\{a^{T(A)}\cos(\phi_{l,m}^T(t) - \alpha^{T(A)}(t)) \\ &\quad + (\gamma_{l,m}^T - \omega^{T(A)})[v^{T(A)}(t)\sin(\phi_{l,m}^T(t) - \alpha^{T(A)}(t))]\}\end{aligned} \tag{34}$$

$$\begin{aligned}&\theta_{l,n}^{R(Z)}(t) \\ &= k_0(\gamma_{l,m}^R - \omega^{R(Z)})^{-2}\{a^{R(Z)}\cos(\phi_{l,n}^R(t) - \alpha^{R(Z)}(t)) \\ &\quad + (\gamma_{l,n}^R - \omega^{R(Z)})[v^{R(Z)}(t)\sin(\phi_{l,n}^R(t) - \alpha^{R(Z)}(t))]\}.\end{aligned} \tag{35}$$

Similarly, the phase shifts associated with the rotations of the Tx and Rx antenna arrays in (12) and (13) can be obtained as

$$\begin{aligned}\varphi_{p,l,m}^T(t) = k_0\Big[&r_{p,x}^T\cos\left(\phi_{l,m}^T(t) - \omega^T t\right) + \\ &r_{p,y}^T\sin\left(\phi_{l,m}^T(t) - \omega^T t\right)\Big]\end{aligned} \tag{36}$$

$$\begin{aligned}\varphi_{q,l,n}^R(t) = k_0\Big[&r_{q,x}^R\cos\left(\phi_{l,n}^R(t) - \omega^R t\right) + \\ &r_{q,y}^R\sin\left(\phi_{l,n}^R(t) - \omega^R t\right)\Big].\end{aligned} \tag{37}$$

Let δ_p and δ_q denote the distances of A_1^T-A_p^T and A_1^R-A_q^R, respectively, i.e., $\mathbf{r}^T = [\delta_p\cos(\beta^T), \delta_p\sin(\beta^T)]$, $\mathbf{r}^R = [\delta_q\cos(\beta^R), \delta_q\sin(\beta^R)]$, the phase shifts in (36) and (37) can be rewritten as

$$\varphi_{p,l,m}^T(t) = k_0\delta_p\cos(\phi_{l,m}^T(t) - \beta^T(t)) \tag{38}$$

$$\varphi_{q,l,n}^R(t) = k_0\delta_q\cos(\phi_{l,n}^R(t) - \beta^R(t)) \tag{39}$$

where $\beta^T(t) = \beta^T + \omega^T t$, $\beta^R(t) = \beta^R + \omega^R t$.

The delay of the l-th path $\tau_l(t)$ is obtained as (15), where the travel distances of the first and last bounces, i.e., $d_{l,m}^T(t)$ and $d_{l,n}^R(t)$ can be simplified as

$$d_l^T(t) \approx d_l^T + v_0^A t\cos(\alpha_0^A - \phi_l^T) - v_0^T t\cos(\alpha_0^T - \phi_l^T) \tag{40}$$

$$d_l^R(t) \approx d_l^R + v_0^Z t\cos(\alpha_0^Z - \phi_l^R) - v_0^R t\cos(\alpha_0^R - \phi_l^R) \tag{41}$$

where $\phi_l^T = \mathbb{E}\{\phi_{l,m}^T\}$ and $\phi_l^R = \mathbb{E}\{\phi_{l,n}^R\}$. Substituting $\tau_l(t)$ into (16) and (17) results in time-varying cluster powers $P_l(t)$.

2) FOR THE LOS COMPONENT

Considering the far distance between the Tx and Rx, $\phi^R_{\mathrm{LoS}}(t) \approx \pi$, phase changes resulting from the relatively movements between the Tx/Rx and scatterers, i.e., $\theta_{\mathrm{LoS}}(t) = \theta^T_{\mathrm{LoS}}(t) + \theta^R_{\mathrm{LoS}}(t)$ can be approximated as

$$\theta^T_{\mathrm{LoS}}(t) \approx -\frac{k_0}{(\omega^T)^2}[a^T \cos(\alpha^T(t)) + \omega^T v^T_0(t) \sin(\alpha^T(t))] \tag{42}$$

$$\theta^R_{\mathrm{LoS}}(t) \approx -\frac{k_0}{(\omega^R)^2}[a^R \cos(\alpha^R(t)) + \omega^R v^R_0(t) \sin(\alpha^R(t))]. \tag{43}$$

The phases associated with the antenna array rotations, i.e., $\varphi_{qp,\mathrm{LoS}}(t)$ can be obtained as

$$\begin{aligned}\varphi_{qp,\mathrm{LoS}}(t) &\approx k_0 \left[r^T_{p,x} \cos\left(\omega^T t\right) - r^T_{p,y} \sin\left(\omega^T t\right)\right. \\ &\quad \left. + r^R_{q,y} \sin\left(\omega^R t\right) - r^R_{q,x} \cos\left(\omega^R t\right)\right] \\ &= k_0[\delta_p \cos(\beta^T(t)) - \delta_q \cos(\beta^R(t))].\end{aligned} \tag{44}$$

The time-varying delay of the LoS path can be simplified as

$$D(t) \approx [D + v^R_0 t \cos(\alpha^R_0) - v^T_0 t \cos(\alpha^T_0)]/c_0. \tag{45}$$

III. STATISTICAL PROPERTIES OF THE NON-STATIONARY MULTI-MOBILITY CHANNEL MODEL

A. LOCAL ST-CCF

The local spatial-temporal CCF (ST-CCF) between two arbitrary CIRs $h_{qp}(t, \tau)$ and $h_{\tilde{q}\tilde{p}}(t', \tau)$ is defined as [39]

$$\rho_{qp,\tilde{q}\tilde{p}}(t, \tau, \Delta\mathbf{r}, \Delta t) = \frac{\mathbb{E}\{h_{qp}(t, \tau) h^*_{\tilde{q}\tilde{p}}(t', \tau)\}}{\sqrt{\mathbb{E}[|h_{qp}(t, \tau)|^2]\mathbb{E}[|h_{\tilde{q}\tilde{p}}(t', \tau)|^2]}} \tag{46}$$

where $t' = t - \Delta t$, $\Delta\mathbf{r} = [\Delta r^T, \Delta r^R]$, including the antenna spacing on the Tx array $\Delta r^T = \left\|\mathbf{r}^T_{\tilde{p}} - \mathbf{r}^T_p\right\|$ and the antenna spacing on the Rx array $\Delta r^R = \left\|\mathbf{r}^R_{\tilde{q}} - \mathbf{r}^R_q\right\|$, $(\cdot)^*$ is the complex conjugate operation. It is assumed that there is no correlation between different clusters. By substituting (1) into (46), $\rho_{qp,\tilde{q}\tilde{p}}(t, \tau, \Delta\mathbf{r}, \Delta t)$ can be further expressed as

$$\begin{aligned}&\rho_{qp,\tilde{p}\tilde{q}}(t, \tau, \Delta\mathbf{r}, \Delta t) \\ &\quad = \frac{K}{K+1}\rho^{\mathrm{LoS}}_{qp,\tilde{p}\tilde{q}}(t, \Delta\mathbf{r}, \Delta t)\delta(\tau - \tau^{\mathrm{LoS}}) \\ &\qquad + \frac{1}{K+1}\sum_{l=1}^{L}\rho^{\mathrm{NLoS}}_{qp,\tilde{p}\tilde{q},l}(t, \Delta\mathbf{r}, \Delta t)\delta(\tau - \tau_l)\end{aligned} \tag{47}$$

where the LoS component of the ST-CCF is given by

$$\begin{aligned}\rho^{\mathrm{LoS}}_{qp,\tilde{p}\tilde{q}}(t, \Delta\mathbf{r}, \Delta t) &= \Pi_{T_0}(t)\Pi_{T_0}(t') \exp\{j[\theta_{\mathrm{LoS}}(t) \\ &\quad + \varphi_{pq,\mathrm{LoS}}(t) - \theta_{\mathrm{LoS}}(t') - \varphi_{\tilde{p}\tilde{q},\mathrm{LoS}}(t')]\}.\end{aligned} \tag{48}$$

Here, the azimuth and elevation angles are jointly described by the VMF distribution, which can provide a good consistency with the measurement data [40], [41]. The probability density function (PDF) of the VMF distribution is defined as

$$\begin{aligned}p(\psi, \phi) = \frac{\kappa \cos(\psi)}{4\pi \sinh(\kappa)} &\exp\{\kappa(\cos(\psi)\cos(\overline{\psi})\cos(\phi - \overline{\phi}) \\ &+ \sin(\psi)\sin(\overline{\psi}))\}\end{aligned} \tag{49}$$

where $\psi \in [-\pi/2, \pi/2]$, $\phi \in [-\pi, \pi]$, $\overline{\psi}$ and $\overline{\phi}$ stand for the mean values of elevation angle ψ and azimuth angle ϕ, respectively, κ controls the angular spread around the mean direction. Considering the independence of the first and last bounce propagaions, the NLoS components of the ST-CCF can be rewritten as

$$\begin{aligned}\rho^{\mathrm{NLoS}}_{qp,\tilde{q}\tilde{q},l}(t, \Delta\mathbf{r}, \Delta t) &= \Pi_{T_0}(t)\Pi_{T_0}(t') \cdot \rho^{\mathrm{T}}_{p\tilde{p},l}(t, \Delta r^T, \Delta t) \\ &\quad \cdot \rho^{\mathrm{R}}_{q\tilde{q},l}(t, \Delta r^R, \Delta t)\end{aligned} \tag{50}$$

where

$$\begin{aligned}&\rho^{\mathrm{T}}_{p\tilde{p},l}(t, \Delta r^T, \Delta t) \\ &\quad = \int_{-\frac{\pi}{2}}^{\frac{\pi}{2}}\int_{-\pi}^{\pi} \exp(j[\theta_{l,m}(t) + \varphi_{p,l,m}(t) \\ &\qquad - \theta_{l,m}(t') - \varphi_{\tilde{p},l,m}(t')])p(\psi^T, \phi^T)\mathrm{d}\psi^T\mathrm{d}\phi^T\end{aligned} \tag{51}$$

$$\begin{aligned}&\rho^{\mathrm{R}}_{q\tilde{q},l}(t, \Delta r^R, \Delta t) \\ &\quad = \int_{-\frac{\pi}{2}}^{\frac{\pi}{2}}\int_{-\pi}^{\pi} \exp(j[\theta_{l,n}(t) + \varphi_{q,l,n}(t) \\ &\qquad - \theta_{l,n}(t') - \varphi_{\tilde{q},l,n}(t')])p(\psi^R, \phi^R)\mathrm{d}\psi^R\mathrm{d}\phi^R.\end{aligned} \tag{52}$$

1) LOCA TEMPORAL ACF

By imposing $p = \tilde{p}$ and $q = \tilde{q}$ in (48) and (50), the LoS and NLoS components of the temporal ACF are obtained as

$$\begin{aligned}\rho^{\mathrm{LoS}}_{qp}(t, \Delta t) &= \Pi_{T_0}(t)\Pi_{T_0}(t') \exp\{j[\theta_{\mathrm{LoS}}(t) \\ &\quad + \varphi_{pq,\mathrm{LoS}}(t) - \theta_{\mathrm{LoS}}(t') - \varphi_{pq,\mathrm{LoS}}(t')]\}\end{aligned} \tag{53}$$

$$\rho^{\mathrm{NLoS}}_{qp,l}(t, \Delta t) = \Pi_{T_0}(t)\Pi_{T_0}(t') \cdot \rho^{\mathrm{T}}_{p,l}(t, \Delta t) \cdot \rho^{\mathrm{R}}_{q,l}(t, \Delta t) \tag{54}$$

where

$$\begin{aligned}\rho^{\mathrm{T}}_{p,l}(t, \Delta t) = &\int_{-\frac{\pi}{2}}^{\frac{\pi}{2}}\int_{-\pi}^{\pi} \exp(j[\theta_{l,m}(t) + \varphi_{p,l,m}(t) \\ &- \theta_{l,m}(t') - \varphi_{p,l,m}(t')])p(\psi^T, \phi^T)\mathrm{d}\psi^T\mathrm{d}\phi^T\end{aligned} \tag{55}$$

$$\begin{aligned}\rho^{\mathrm{R}}_{q,l}(t, \Delta t) = &\int_{-\frac{\pi}{2}}^{\frac{\pi}{2}}\int_{-\pi}^{\pi} \exp(j[\theta_{l,n}(t) + \varphi_{q,l,n}(t) \\ &- \theta_{l,n}(t') - \varphi_{q,l,n}(t')])p(\psi^R, \phi^R)\mathrm{d}\psi^R\mathrm{d}\phi^R.\end{aligned} \tag{56}$$

For the 2D multi-mobility model, the VMF distribution reduces to von Mises (VM) distribution, i.e., $p(\phi) = \exp\{\kappa\cos(\phi - \overline{\phi})\}/\{2\pi I_0(\kappa)\}$, $\phi \in [-\pi, \pi)$, $I_0(\cdot)$ is the zero order modified Bessel function of the first kind.

By substituting (34), (35), (38), and (39) into (55) and (56), and using [42, eq. (3.338)–(4)], temporal ACFs on the Tx and Rx sides can be obtained as the following closed-form expressions

$$\rho^{\mathrm{T}}_{p,l}(t,\Delta t) = I_0\{[(\Omega^T_1(t,t')-\Omega^{A_l}_1(t,t')+\Psi^T_1(t,t'))^2 + (\Omega^T_2(t,t')-\Omega^{A_l}_2(t,t')+\Psi^T_2(t,t'))^2]^{\frac{1}{2}}\}/I_0(\kappa^T) \tag{57}$$

$$\rho^{\mathrm{R}}_{q,l}(t,\Delta t) = I_0\{[(\Omega^R_1(t,t')-\Omega^{Z_l}_1(t,t')+\Psi^R_1(t,t'))^2 + (\Omega^R_2(t,t')-\Omega^{Z_l}_2(t,t')+\Psi^R_2(t,t'))^2]^{\frac{1}{2}}\}/I_0(\kappa^R) \tag{58}$$

where

$$\Omega^X_1(t,t') = \frac{jk_0a^X}{(\gamma^X_l-\omega^X)^2}[\mathcal{A}^X(t)-\mathcal{A}^X(t')] + \frac{jk_0}{\gamma^X_l-\omega^X}[v^X(t')\mathcal{B}^X(t')-v^X(t)\mathcal{B}^X(t)] \tag{59}$$

$$\Omega^X_2(t,t') = \frac{jk_0a^X}{(\gamma^X_l-\omega^X)^2}[\mathcal{B}^X(t)-\mathcal{B}^X(t')] + \frac{jk_0}{\gamma^Y_l-\omega^X}[v^X(t)\mathcal{A}^X(t)-v^X(t')\mathcal{A}^X(t')] \tag{60}$$

$$\Psi^{T(R)}_1(t,t') = jk_0\delta_{p(q)}[\mathcal{C}^{T(R)}(t)-\mathcal{C}^{T(R)}(t')]+\kappa^{T(R)}\cos(\overline{\phi}^{TR}) \tag{61}$$

$$\Psi^{T(R)}_2(t,t') = jk_0\delta_{p(q)}[\mathcal{D}^{T(R)}(t)-\mathcal{D}^{T(R)}(t')]+\kappa^{T(R)}\sin(\overline{\phi}^{TR}). \tag{62}$$

Here, $X \in \{T,R,A_l,Z_l\}$, $\mathcal{A}^{T(A_l)}(t) = \cos(\alpha^{T(A_l)}(t)-\gamma^T_l t)$, $\mathcal{A}^{R(Z_l)}(t) = \cos(\alpha^{R(Z_l)}(t)-\gamma^R_l t)$, $\mathcal{B}^{T(A_l)}(t) = \sin(\alpha^{T(A_l)}(t)-\gamma^T_l t)$, $\mathcal{B}^{R(Z_l)}(t) = \sin(\alpha^{R(Z_l)}(t)-\gamma^R_l t)$, $\mathcal{C}^{T(R)}(t)=\cos(\beta^{T(R)}(t)-\gamma^{T(R)}_l t)$, $\mathcal{D}^{T(R)}(t)=\sin(\beta^{T(R)}(t)-\gamma^{T(R)}_l t)$, $\gamma^T_{l,m}\approx\gamma^T_l$, and $\gamma^R_{l,n}\approx\gamma^R_l$ due to the small angular spread. It is worth noting that the temporal ACF is time-varying according to the dynamic scattering environment and can capture the impacts of speed and trajectory variations of the Tx, Rx, and scatterers as well as the antenna rotations on both sides.

2) LOCAL SPATIAL CCF

Let $t = t'$ in (48) and (50), the LoS and NLoS components of local spatial CCF are given by

$$\rho^{\mathrm{LoS}}_{qp,\tilde{p}\tilde{q}}(t,\Delta\mathbf{r}) = \Pi_{T_0}(t)\exp\{j[\varphi_{pq,\mathrm{LoS}}(t)-\varphi_{\tilde{p}\tilde{q},\mathrm{LoS}}(t)]\} \tag{63}$$

$$\rho^{\mathrm{NLoS}}_{qp,\tilde{q}\tilde{p},l}(t,\Delta\mathbf{r}) = \Pi_{T_0}(t)\cdot\rho^{\mathrm{T}}_{p\tilde{p},l}(t,\Delta r^T)\cdot\rho^{\mathrm{R}}_{q\tilde{q},l}(t,\Delta r^R) \tag{64}$$

where

$$\rho^T_{p\tilde{p},l}(t,\delta^T) = \int_{-\frac{\pi}{2}}^{\frac{\pi}{2}}\int_{-\pi}^{\pi}\exp(j[\varphi_{p,l,m}(t)-\varphi_{\tilde{p},l,m}(t)]) \times p(\psi^T,\phi^T)\mathrm{d}\psi^T\mathrm{d}\phi^T \tag{65}$$

$$\rho^R_{q\tilde{q},l}(t,\delta^R) = \int_{-\frac{\pi}{2}}^{\frac{\pi}{2}}\int_{-\pi}^{\pi}\exp(j[\varphi_{q,l,n}(t)-\varphi_{\tilde{q},l,n}(t)]) \times p(\psi^R,\phi^R)\mathrm{d}\psi^R\mathrm{d}\phi^R. \tag{66}$$

For the 2D multi-mobility model, by using [42, eq. (3.338)–(4)], $\rho^{\mathrm{NLoS}}_{qp,\tilde{q}\tilde{p},l}(t,\Delta\mathbf{r})$ can be obtained as the following closed-form expression

$$\rho^{\mathrm{NLoS}}_{qp,\tilde{p}\tilde{q},l}(t,\Delta\mathbf{r}) = \frac{\Pi_{T_0}(t)}{I_0(\kappa^T)I_0(\kappa^R)}I_0\{[\Gamma^T(\delta_p)^2+\Lambda^T(\delta_p)^2]^{\frac{1}{2}}\} \times I_0\{[\Gamma^R(\delta_q)^2+\Lambda^R(\delta_q)^2]^{\frac{1}{2}}\} \tag{67}$$

where

$$\Gamma^{T(R)}\left(\delta_{p(q)}\right) = jk_0\delta_{p(q)}\mathcal{C}^{T(R)}(t)+\kappa^{T(R)}\cos\overline{\phi}^{TR} \tag{68}$$

$$\Lambda^{T(R)}\left(\delta_{p(q)}\right) = jk_0\delta_{p(q)}\mathcal{D}^{T(R)}(t)+\kappa^{T(R)}\sin\overline{\phi}^{TR}. \tag{69}$$

Finally, the LoS component of the local spatial CCF is reduced to

$$\rho^{\mathrm{LoS}}_{qp,\tilde{q}\tilde{q}}(t,\Delta\mathbf{r}) = \Pi_{T_0}(t)\exp\{jk_0[\delta^R\cos(\beta^R(t)) - \delta^T\cos(\beta^T(t))]\}. \tag{70}$$

B. LOCAL DOPPLER PSD

The local Doppler PSD of the proposed model can be obtained by applying the Fourier transform to the temporal ACF with respect to Δt, i.e.,

$$S_{qp}(t,\tau,f) = \int_{-\infty}^{\infty}\rho_{qp}(t,\tau,\Delta t)e^{-j2\pi f\Delta t}\mathrm{d}\Delta t = \frac{K}{K+1}S^{\mathrm{LoS}}_{qp}(t,f)\delta(\tau-\tau^{\mathrm{LoS}}) + \frac{1}{K+1}\sum_{l=1}^{L}S^{\mathrm{NLoS}}_{qp,l}(t,f)\delta(\tau-\tau_l). \tag{71}$$

By substituting (54) into (71), the NLoS components of the local Doppler PSD can be obtained as

$$S^{\mathrm{NLoS}}_{qp,l}(t,f) = T_0\Pi_{T_0}(t)\exp\{-j2\pi f(t-T_0/2)\}\mathrm{sinc}\{T_0\pi f\} \odot\mathcal{F}\{\rho^T_{p,l}(t,\Delta t)\}\odot\mathcal{F}\{\rho^R_{q,l}(t,\Delta t)\} \tag{72}$$

where $\odot$ designates convolution and $\mathcal{F}\{\cdot\}$ denotes the Fourier transformation in terms of Δt. Similarly, the LoS component of the local Doppler PSD is calculated as

$$S^{\mathrm{LoS}}_{qp}(t,f) = T_0\Pi_{T_0}(t)\exp\{-j2\pi f(t-T_0/2)\}\mathrm{sinc}\{T_0\pi f\} \odot\mathcal{F}\{\exp\{j[\theta_{\mathrm{LoS}}(t)+\varphi_{pq,\mathrm{LoS}}(t)-\theta_{\mathrm{LoS}}(t') - \varphi_{pq,\mathrm{LoS}}(t')]\}\}. \tag{73}$$

C. ST-DOPPLER FREQUENCY

The instantaneous frequency of a signal is defined as the derivative of its phase with respect to time [43]. In the proposed model, the instantaneous Doppler frequencies stem from two effects, i.e., the movements of the Tx, Rx, and scatterers, and the antenna array rotations on both sides. Based on (2), the total instantaneous Doppler frequency of a multipath component via C_l^A and C_l^Z can be calculated as

$$f_{qp,l,mn}(t) = \frac{1}{2\pi}\frac{\mathrm{d}[\theta_{l,mn}(t) + \varphi_{qp,l,mn}(t)]}{\mathrm{d}t} \tag{74}$$

and can be further expressed as

$$f_{qp,l,mn}(t) = f^T_{p,l,m}(t) + f^R_{p,l,n}(t) \tag{75}$$

where

$$f^T_{p,l,m}(t) = \frac{1}{2\pi}\frac{\mathrm{d}[\theta^{T/A_l}_{l,m}(t) + \varphi^T_{p,l,m}(t)]}{\mathrm{d}t} \tag{76}$$

$$f^R_{q,l,n}(t) = \frac{1}{2\pi}\frac{\mathrm{d}[\theta^{R/Z_l}_{l,n}(t) + \varphi^R_{q,l,n}(t)]}{\mathrm{d}t}. \tag{77}$$

The Tx and Rx sides of the instantaneous Doppler frequencies of the 2D multi-mobility model can be obtained as

$$f^T_{p,l,m}(t) = \underbrace{f^T_{l,m}(t) - f^{A_l}_{l,m}(t)}_{\text{Tx and } C_l^A \text{ movements}} + \underbrace{\frac{\delta_p}{\lambda}(\gamma^T_{l,m} - \omega^T)\sin[\phi^T_{l,n}(t) - \beta^T(t)]}_{\text{Tx array rotation}} \tag{78}$$

$$f^R_{q,l,n}(t) = \underbrace{f^R_{l,n}(t) - f^{Z_l}_{l,n}(t)}_{\text{Rx and } C_l^Z \text{ movements}} + \underbrace{\frac{\delta_q}{\lambda}(\gamma^R_{l,n} - \omega^R)\sin[\phi^R_{l,m}(t) - \beta^R(t)]}_{\text{Rx array rotation}}. \tag{79}$$

Similarly, the instantaneous Doppler frequencies of the LoS path can be expressed as

$$f_{\mathrm{LoS}}(t) = \underbrace{f^R_{\mathrm{LoS}}(t) + f^T_{\mathrm{LoS}}(t)}_{\text{Tx and Rx movements}} - \underbrace{\frac{\delta_p}{\lambda}\omega^T\sin[\beta^T(t)] + \frac{\delta_q}{\lambda}\omega^R\sin[\beta^R(t)]}_{\text{Tx and Rx arrays rotation}} \tag{80}$$

where $f^R_{\mathrm{LoS}}(t) = -v^R(t)/\lambda\cos(\alpha^R(t))$, $f^T_{\mathrm{LoS}}(t) = -v^T(t)/\lambda\cos(\alpha^T(t))$.

The instantaneous Doppler frequencies in (78)–(80) provide physical insight into time variation of the proposed channel model. Due to the symmetry of the instantaneous Doppler frequencies on the two sides, only the Tx side is analyzed. In (78), the first two terms account for the time-varying Doppler frequencies caused by the movements of the Tx and C_l^A. The third term is caused by the Tx array rotation. It should be noticed that when the Tx and C_l^A move with constant speeds in certain directions, the third term still exist due to the time variation rate of AoDs, i.e., $\gamma^T_{l,m}$. If the WSS and constant velocity assumptions are considered, (78) reduces to the conventional time-invariant Doppler frequencies as

$$f_{l,m} = \frac{v^T_0}{\lambda}\cos(\phi^T_{l,m} - \alpha^T_0) - \frac{v^{A_l}_0}{\lambda}\cos(\phi^T_{l,m} - \alpha^{A_l}_0). \tag{81}$$

Similar analysis can be applied to the Doppler frequencies on the Rx sides in (79). Note that the instantaneous Doppler frequencies in (78)–(80) are different from those in [26], which cannot capture the impacts of time-varying angles, array rotations, and scatterer movements. The local Doppler spread of the NLoS components can be calculated as

$$B_D(t) = \left(\mathbb{E}[f_{qp,l,mn}(t)^2] - \{\mathbb{E}[f_{qp,l,mn}(t)]\}^2\right)^{\frac{1}{2}}. \tag{82}$$

Another way of estimating the instantaneous Doppler frequencies is to apply the time-frequency analysis to complex channel gain, e.g., using the short-time Fourier transform (STFT). The STFT of the l-th cluster can be expressed as

$$H_{qp,l}(t,f) = \int_{-\infty}^{\infty} h_{qp,l}(u)g^*(u-t)e^{-j2\pi fu}\mathrm{d}u \tag{83}$$

where $g(t)$ is the window function, e.g., rectangular window function, Hamming window function, etc. Similarly, for the LoS path, its STFT can be expressed as

$$H^{\mathrm{LoS}}_{qp}(t,f) = \int_{-\infty}^{\infty} h^{\mathrm{LoS}}_{qp}(u)g^*(u-t)e^{-j2\pi fu}\mathrm{d}u. \tag{84}$$

D. STATIONARY INTERVAL

The stationary interval is the longest time interval within which the channel can be considered as WSS. It provides a measure of time-variation characteristics of non-stationary channels [44]. Several methods have been proposed to measure the stationary interval of non-stationary channels, such as correlation matrix distance (CMD) [9], local region of stationarity (LRS) [45], and spectral divergence (SD) [46]. The CMD measures the time-variation of spatial structure of the channel. It is defined as the distance between two channel correlation matrices. Similarly, the SD quantizes the distance between two spectral densities of the channel. The LRS characterizes channel non-stationarity from the point of view of channel power variation. It is defined as the longest time interval within which the correlation coefficient of two averaged power delay profiles (APDPs) is over a given threshold. Here, the channel non-stationarity is estimated from the time variation of the Doppler spread [47]. The stationary interval is defined as the maximum time duration within which the relative error of Doppler spread beyond a certain threshold, i.e.,

$$T_c = \max\{\Delta t \mid \epsilon(\Delta t) \geqslant c\} \tag{85}$$

where

$$\epsilon(\Delta t) = \frac{|B_D(\Delta t) - B_D(0)|}{B_D(0)}. \tag{86}$$

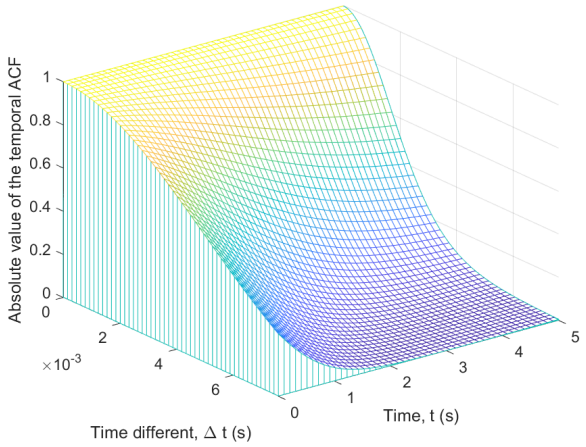

FIGURE 3. Absolute value of the local temporal ACFs of the multi-mobility channel model ($v_0^{T(R)} = 30$ km/h, $\alpha_0^{T(R)} = \pi/4$, $a^{T(R)} = 1$ m/s^2, and $\omega^{T(R)} = \pi/20$ s^{-1}).

IV. RESULTS AND ANALYSIS

In this section, the theoretical results of the statistical properties are compared with approximate and simulated results and validated by the corresponding measurement data. In the simulation, the observation time interval is [0, 5 s]. For simplicity, uniform linear arrays are used in analysis. The antenna spacings of the Tx and Rx arrays are δ^T and δ^R, respectively. Thus, the distances of A_1^T-A_p^T and A_1^R-A_q^R are $\delta_p = \delta^T(p-1)$ and $\delta_q = \delta^R(q-1)$, respectively. Unless otherwise stated, both the C_l^A and C_l^Z are moving with the speed of 30 km/h along the x-axis. Other basic parameters are set as follows: $f_c = 5.9$ GHz, $\delta^{T(R)} = \lambda/2$, $\tilde{p}(\tilde{q}) = 2$, $p(q) = 1$, $\beta_0^{T(R)} = \pi/3$, $\kappa^{T(R)} = 15$, $\overline{\phi}^T = \pi/6$, $\overline{\phi}^R = 2\pi/3$, $d^{T(R)} = 200$ m. Besides, the horizontal propagations are assumed in the simulation. For simplicity, omnidirectional antennas are used and only vertical polarization is considered.

Fig. 3 illustrates the absolute value of the time-varying local temporal ACFs. Both the Tx and Rx are moving with an acceleration, i.e., $a^{T(R)} = 1$ m/s^2 and angular speed, i.e., $\omega^{T(R)} = \pi/20$ s^{-1}. It is obvious that the temporal correlation of the proposed channel model decreases over time, which is in contrast to the WSS case. The time variations of the temporal correlation are caused by the relative movements of the Tx and Rx with respective to the first and last bounce clusters, respectively. In order to illustrate more clearly, Fig. 4 shows the theoretical, approximated, and simulated absolute values of the local temporal ACFs for three scenarios at $t = 1$ s. In scenario I, the Tx and Rx travel with constant velocities in given directions, i.e., $a^{T(R)} = 0$ m/s^2, $\omega^{T(R)} = 0$ s^{-1}. In scenario II, the Tx and Rx travel with constant velocities but time-varying moving directions, i.e., $a^{T(R)} = 0$ m/s^2, $\omega^{T(R)} = \pi/20$ s^{-1}. For scenario III, both the speeds and moving directions of the Tx and Rx are changing, i.e., $a^{T(R)} = 1$ m/s^2, $\omega^{T(R)} = \pi/20$ s^{-1}. Compared with the constant velocity case, i.e., scenario I, time-varying travel angles of the Tx and Rx result in weaker temporal correlations of the model. Scenarios III represents a high-mobility scattering environment, where both the Tx and Rx move with accelerations and angular speeds, resulting in the lowest temporal correlations of the model. An excellent agreement between the theoretical, approximated, and simulated results verifies the correctness of the derivations and simulations.

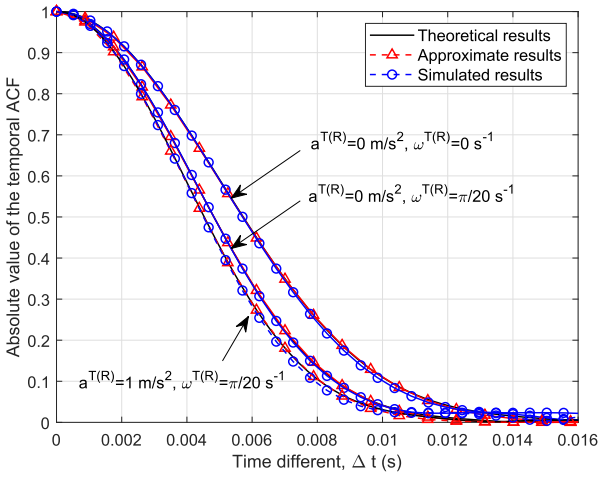

FIGURE 4. The theoretical, approximate, and simulated absolute values of the local temporal ACFs of the multi-mobility channel model for three non-stationary scenarios ($t = 1$ s, $v_0^{T(R)} = 30$ km/h, and $\alpha_0^{T(R)} = \pi/4$).

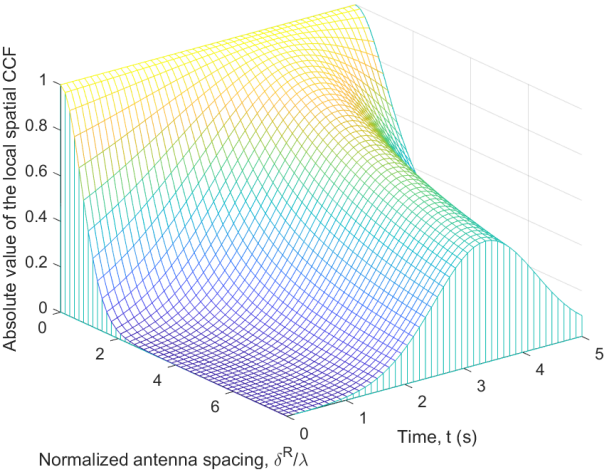

FIGURE 5. Absolute value of the local spatial CCFs of the multi-mobility channel model ($v_0^R = 30$ km/h, $\alpha_0^R = \pi/4$, $a^R = 1$ m/s^2, and $\omega^R = \pi/10$ s^{-1}).

Fig. 5 illustrates the absolute value of the time-varying local spatial CCFs at the Rx side. The Rx antenna spacing has been normalized in terms of the wavelength. On the Tx sides, imposing $p = \tilde{p}$ means two links share the same Tx antenna. The result is obtained when the Rx moves with an acceleration $a^R = 1$ m/s^2 and angular speed $\omega^R = \pi/10$ s^{-1}. Equation (67) indicates that spatial correlation of the proposed model depends on the time-varying AoAs (AoDs) and the Rx(Tx) array tilt angle. In this figure, the maximum values of the spatial correlation on time axis are obtained when the central arrival ray and the Rx array are parallel to each other. If the time variation of AoAs is neglected due to the short observation interval, the maximum values of spatial correlation appear at $|\overline{\phi}^R - \beta_0^R|/(\omega^R) \approx 3.33$ s. Note that

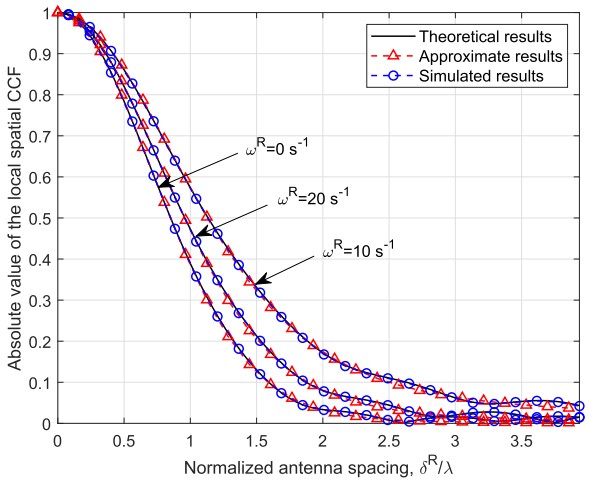

FIGURE 6. The theoretical, approximate, and simulated absolute values of the local spatial CCFs of the multi-mobility channel model with different angular speeds of the Rx ($t = 1$ s, $v_0^R = 30$ km/h, $\alpha_0^R = \pi/4$, and $a^R = 1$ m/s^2).

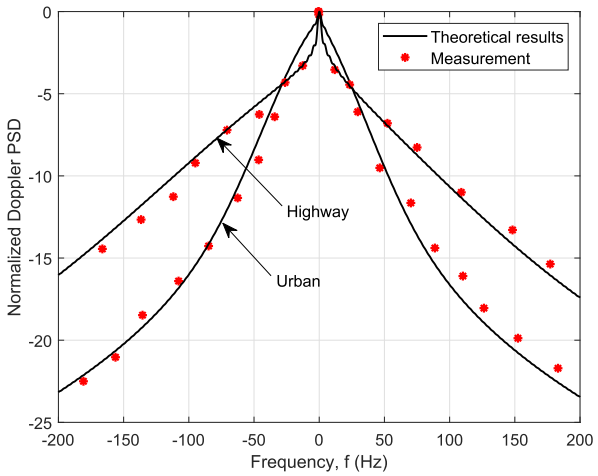

FIGURE 7. Comparison between the normalized local Doppler PSD of the multi-mobility channel model and the measurement data in [48] ($f_c = 5.2$ GHz, $\bar{\phi}^{T(R)} = \pi/5$, $\alpha_0^{T(A)} = 0$, $\alpha_0^{R(Z)} = \pi$, and $d^{T(R)} = 100$ m, urban scenario: $\kappa^{T(R)} = 10$, $v_0^{T(R)} = 36$ km/h, $v_0^{A(Z)} = 54$ km/h, highway scenario: $\kappa^{T(R)} = 6$, $v_0^{T(R)} = 54$ km/h, and $v_0^{A(Z)} = 90$ km/h).

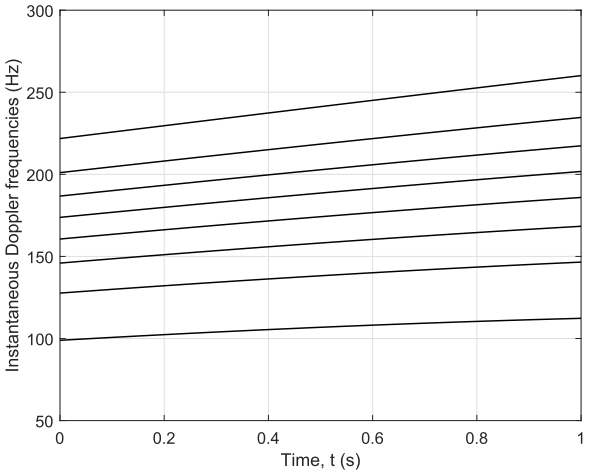

FIGURE 8. Instantaneous Doppler frequencies of the multi-mobility channel model ($v_0^{T(R)} = 30$ km/h, $\alpha_0^{T(R)} = \pi/3$, $a^{T(R)} = 1$ m/s^2, and $\omega^{T(R)} = \pi/20$ s^{-1}).

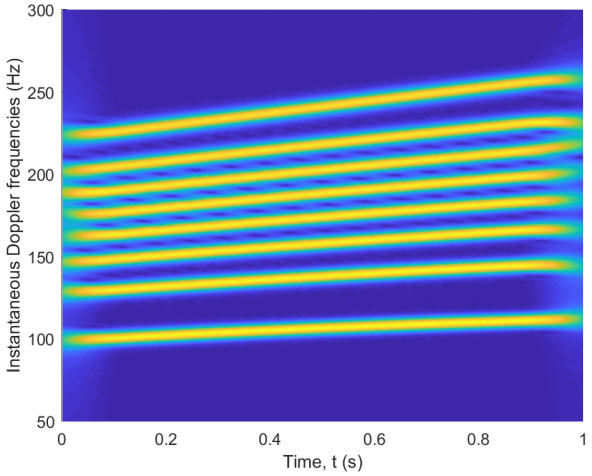

FIGURE 9. STFT of the complex channel gain of the multi-mobility channel model ($v_0^{T(R)} = 30$ km/h, $\alpha_0^{T(R)} = \pi/3$, $a^{T(R)} = 1$ m/s^2, and $\omega^{T(R)} = \pi/20$ s^{-1}).

the influence of the accelerations on the spatial correlation of the model can be neglected by using approximate expressions in (25) and (26). Fig. 6 shows the theoretical, approximate, and simulated absolute values of the local spatial CCFs at $t = 1$ s. The results are obtained with different angular speeds of the Rx, i.e., 0 s^{-1}, $\pi/20$ s^{-1}, $\pi/10$ s^{-1}. The angles between the Rx antenna array and AoAs become smaller when using larger angular speeds, which result in stronger spatial correlation. Again, the theoretical results match the approximate and simulated results very well, illustrating the correctness of derivations and simulations.

Fig. 7 shows the normalized local Doppler PSD of the proposed channel model and the corresponding measurement data in [48]. The V2V channel measurements were carried out at 5.2 GHz in urban and highway scenarios. According to the measurement campaigns in [48], the model parameters for urban scenarios are: $\kappa^{T(R)} = 10$, $v_0^{T(R)} = 36$ km/h, and $v_0^{A(Z)} = 54$ km/h. For the highway scenario, the model parameters are set as: $\kappa^{T(R)} = 6$, $v_0^{T(R)} = 54$ km/h, and $v_0^{A(Z)} = 90$ km/h. The Tx, Rx, and scatterers are assumed to move with constant velocities. Compared with the Doppler PSD in urban scenario, the Doppler PSD in highway is broader, which is resulted from the larger Doppler spread and higher relative speeds between the Tx and Rx. The close agreement between the theoretical results and the corresponding measurement data confirms the usefulness of the proposed channel model.

The instantaneous Doppler frequencies according to (74) and the STFT of the complex channel gain are shown in Figs. 8 and 9, respectively. In the STFT, the Hamming window function was used with a window length of 0.25 s. A total of 8 rays were generated. It can be observed that the instantaneous Doppler frequencies drift to higher values over time as the result of relative movements between the

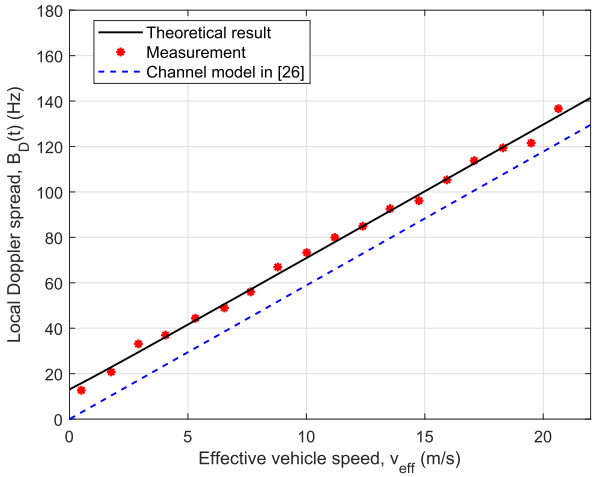

FIGURE 10. The local Doppler spread of the multi-mobility channel model, the model in [26], and the measurement data in [49] ($\kappa^{T(R)} = 10$, $\overline{\phi}^{T} = \pi/3$, $\overline{\phi}^{R} = 5\pi/6$, $v_0^{T(R)} = 30$ km/h, $\alpha_0^{T(R)} = \pi/6$, $a^{T(R)} = 0$ m/s^2, $\omega^{T(R)} = 0$ s^{-1}, $v_0^{A} = 15$ km/h, and $v_0^{Z} = 0$ km/h).

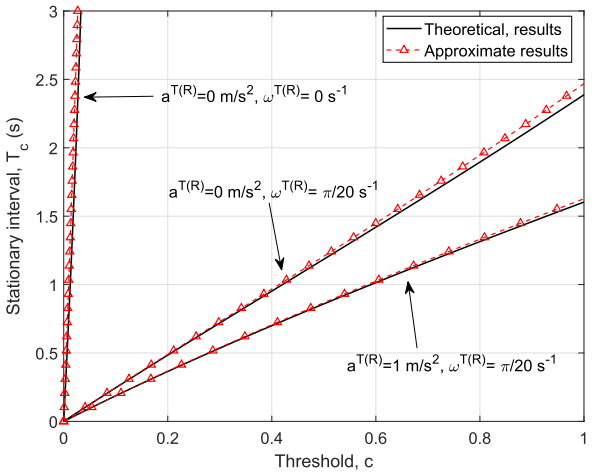

FIGURE 11. Stationary intervals of the multi-mobility channel model with different velocities of the MS ($v_0^{T(R)} = 30$ km/h, $\alpha_0^{T} = 0$, $\alpha_0^{R} = \pi$, $v_0^{A(Z)} = 0$ km/h, and $a^{A(Z)} = 0$ s^{-1}).

Tx/Rx and scatterers, and array rotations, illustrating the non-stationarity of the proposed model. Besides, a good consistency of the instantaneous Doppler frequencies between Fig. 8 and Fig. 9 can be observed, which verifies the correctness of our derivations and simulations.

The comparison of the local Doppler spreads of the proposed model, the model in [26], and the corresponding measurement data [49] is shown in Fig. 10. The V2V channel measurements were conducted at 5.9 GHz in a suburban scenario. It indicated that the Doppler spread illustrates a linear dependence on the effective speed, i.e., $B_D = 0.482/(\sqrt{2}\lambda)v_{\text{eff}} + 11.5$, where the effective speed is defined as $v_{\text{eff}} = \sqrt{(v_0^T)^2 + (v_0^R)^2}$ [49]. In the simulation, the channel parameters are chosen as: $\kappa^{T(R)} = 10$, $\overline{\phi}^{T} = \pi/3$, $\overline{\phi}^{R} = 5\pi/6$, $v_0^{T(R)} = 30$ km/h, $\alpha_0^{T(R)} = \pi/6$, $a^{T(R)} = 0$ m/s^2, $\omega^{T(R)} = 0$ s^{-1}, $v_0^{A} = 15$ km/h, and $v_0^{Z} = 0$ km/h. In this figure, the slope of the local Doppler spread is determined by the scatterers non-isotropic distribution. The nonzero value when $v_{\text{eff}} = 0$, i.e., both Tx and Rx are static, is resulted from the motion of scatterers in the propagation environments. Higher speeds of the moving scatterers lead to larger values of the offset at $v_{\text{eff}} = 0$. The theoretical result of the multi-mobility model fits the corresponding measurement data very well, illustrating the utility of the proposed channel model. Note that the nonzero offset of the local Doppler spread at $v_{\text{eff}} = 0$ cannot be achieved by the channel models assuming fixed scatterers, e.g., the model in [26], which leads to a mismatch with the corresponding measurement data.

The stationary intervals of the proposed channel model with different velocities of the MS are shown in Fig. 11. For the sake of analysis, the scatterers are assumed to be fixed. For a given threshold c, the channel can be assumed as stationary during the time interval $[0, T_c]$. A typical threshold can be set as $c = 0.2$. In the first scenario, where both the Tx and Rx move with constant speeds in given directions. Note that

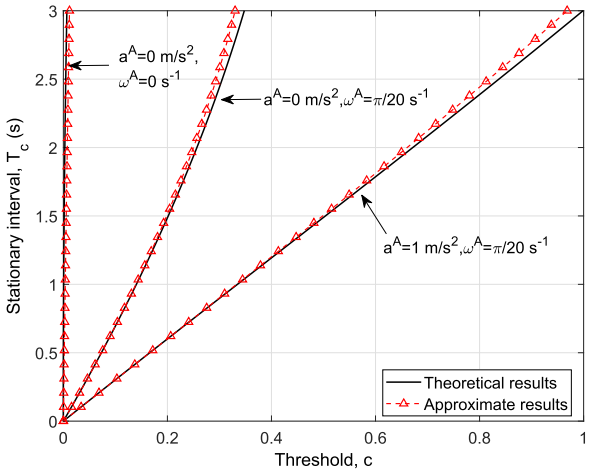

FIGURE 12. Stationary intervals of the multi-mobility channel model with different velocities of scatterers ($v_0^{T(R)} = 30$ km/h, $\alpha_0^{T} = 0$, $\alpha_0^{R} = \pi$, $a^{T(R)} = 0$ m/s^2, $\omega^{T(R)} = 0$ s^{-1}, $v_0^{A(Z)} = 30$ km/h, $a^{Z} = 0$ m/s^2, $\omega^{Z} = 0$ s^{-1}, and $\alpha_0^{A(Z)} = \pi/3$).

the model is still non-stationary. The small angle relative to the y-axis is resulted from the time-varying parameters such as AoDs and AoAs. For the second scenario, the Tx and Rx travel with an angular speed $\pi/20$ s^{-1}, the stationary interval reduced to 0.483 s. In the last scenario, both the Tx and Rx move with time-varying speeds and travel angles, which results in the shortest stationary interval, i.e., 0.367 s. Similarly, the influences of scatterer mobility on the stationarity of the channel are shown in Fig. 12. The stationary interval of the channel is 1.51 s when the scatterers moves with an angular speed. When the scatterers move with time-varying speed and travel angle, which results in a high-mobility scenario, the stationary interval of the channel reduces to 0.621 s. It is obvious that the time-varying speeds and moving directions of the Tx/Rx and scatterers can significantly increase the channel non-stationarity. Note that in [26] and [29], the channel models with constant velocities of the Tx/Rx do not introduce

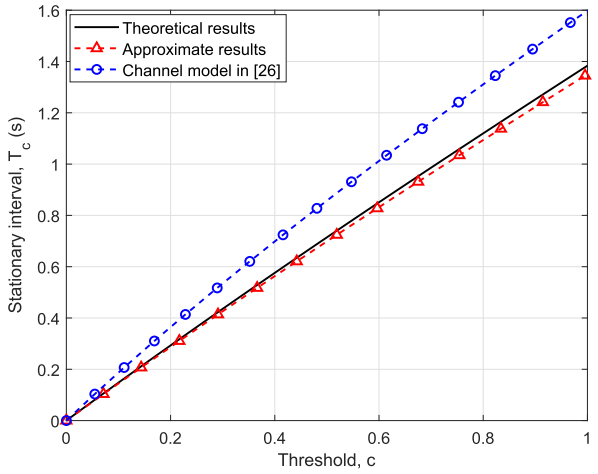

FIGURE 13. Stationary intervals of the multi-mobility channel model and the model in [26] ($v_0^{T(R)} = 30$ km/h, $\alpha_0^T = 0$, $\alpha_0^R = \pi$, $a^{T(R)} = 1$ m/s^2, $\omega^{T(R)} = \pi/20$ s^{-1}, $a^{A(Z)} = 0$ m/s^2, $\omega^{A(Z)} = 0$ s^{-1}, $\alpha^A = \pi/2$, and $\alpha^Z = \pi/3$).

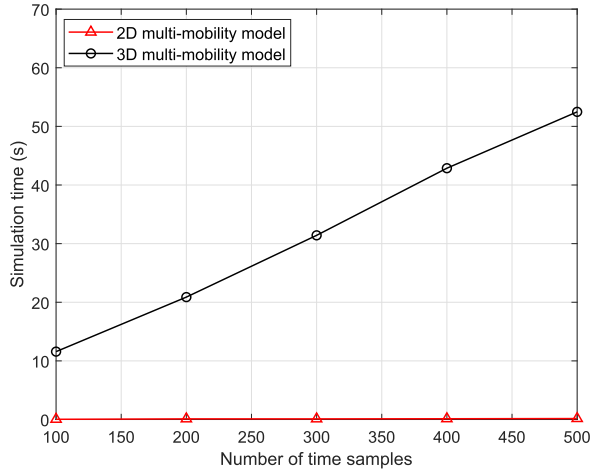

FIGURE 14. Simulation time of the 2D and 3D non-stationary multi-mobility channel models ($M_T = 2$, $M_R = 2$, $L = 16$, $M_l = 5$, $N_l = 5$, $v_0^{T(R)} = 30$ km/h, $\alpha_0^{T(R)} = \pi/4$, $a^{T(R)} = 1$ m/s^2, $\omega^{T(R)} = \pi/20$ s^{-1}, $v_0^{A(Z)} = 30$ km/h, $\alpha_0^{A(Z)} = 0$, $a^{A(Z)} = 1$ m/s^2, and $\omega^{A(Z)} = \pi/20$ s^{-1}).

non-stationarity. The close agreement between the theoretical results and approximate results confirms the accuracy of the approximate expressions during the observation time interval. Furthermore, Fig. 13 shows the comparison between the proposed model and the model in [26] in terms of the stationary interval. Both the Tx and Rx move with the acceleration of 1 m/s^2 and the angular speed of $\pi/20$ s^{-1}. The stationary intervals of the proposed model and the model in [26] when $c = 0.2$ are about 0.291 s and 0.361 s, respectively. The reason for the difference is that the model in [26] neglects the movements of scatterers, and channel parameters such as angles and powers are time-invariant. The non-stationarity of the model only results from the time-varying velocities of the MSs, which may not sufficiently capture the non-stationarity of the V2V channel.

Fig. 14 illustrates the simulation time of the 3D and the corresponding simplified 2D multi-mobility V2V models. A laptop with an Intel Core i5, 2.5 GHz CPU and 8 GB RAM was used for testing. The simulations were conducted considering a 2×2 MIMO system in the urban micro-cell (UMi) scenario under NLoS condition [32]. A total of 16 clusters were generated and each cluster consists of 25 rays. The sampling interval is $\lambda/(4 * v_{\max})$, where $v_{\max}$ is the maximum speed of the Tx/Rx in the simulation. The results show that the simulation time of the simplified 2D multi-mobility model remains nearly constant, i.e., about several tens of milliseconds and only slightly increases as the number of time samples increases. For the 3D multi-mobility model, the simulation time increases significantly with the increase of the number of time samples, i.e., about 11.12 s when the number of time samples is 100 and increase to 52.11 s when the number of time samples is 500. The reason is that for the simplified 2D multi-mobility model, the phases caused by the movement of the Tx, Rx, and scatterers, i.e., $\theta_{l,mn}(t)$, and phases associated with the rotations of antenna arrays on both sides, i.e., $\varphi_{qp,l,mn}(t)$ were obtained as closed-form expressions. However, the above-mentioned phases of the 3D multi-mobility model have to be obtained by carrying out numerical integrations, which are time-consuming processes.

Although the 3D multi-mobility model is more complex than the corresponding 2D model, it is more accurate to capture the characteristics of realistic V2V channels. For scenarios with low elevation angles, e.g., SMa scenario, the 2D multi-mobility model has similar accuracy to that of the corresponding 3D model but is more efficient, and therefore is recommended to be used. Besides, compared with the 3D multi-mobility model, the 2D multi-mobility model with closed-form expressions can yield more insight into the relationship between channel model parameters and statistical properties, e.g., temporal ACF and spatial CCF.

V. CONCLUSIONS

In this paper, a 3D non-stationary multi-mobility V2V channel model has been proposed. The model considers a more general scenario where the Tx, Rx, and scatterers are allowed to move with time-varying speeds and along arbitrary trajectories. The influences of antenna array rotations on channel characteristics have been incorporated. The multi-mobility of the proposed model results in time-varying angles, delays, and powers, which make the model non-stationary. For the scenarios such as RMa and SMa, a highly-efficient 2D multi-mobility model has been proposed, where the closed-form expressions of temporal ACF and spatial CCF are provided. The proposed model can include many existing V2V channel models as special cases or reduce to simple channel models by adjusting channel model parameters properly. The consistency among the theoretical, simulated, and approximate results of the statistics shows the correctness of both derivations and simulations. The usefulness of the proposed model has been validated by comparing the local Doppler PSD and local Doppler spread with the corresponding measurement data. It has been demonstrated that the speed and trajectory variations of the transceiver as well as the moving scatterers

can have remarkable effects on statistical properties of the channel and intensify the channel non-stationarity.

REFERENCES

[1] C.-X. Wang *et al.*, "Cellular architecture and key technologies for 5G wireless communication networks," *IEEE Commun. Mag.*, vol. 52, no. 2, pp. 122–130, Feb. 2014.

[2] V. Nurmela, *METIS Channel Models*, document ICT-317669/D1.4, METIS, Jul. 2015.

[3] C.-X. Wang, J. Bian, J. Sun, W. Zhang, and M. Zhang, "A survey of 5G channel measurements and models," *IEEE Commun. Surveys Tuts.*, vol. 20, no. 4, pp. 3142–3168, 4th Quart., 2018.

[4] K. Zheng, Q. Zheng, P. Chatzimisios, W. Xiang, and Y. Zhou, "Heterogeneous vehicular networking: A survey on architecture, challenges, and solutions," *IEEE Commun. Surveys Tuts.*, vol. 17, no. 4, pp. 2377–2396, 4th Quart., 2015.

[5] X. Cheng, L. Yang, and X. Shen, "D2D for intelligent transportation systems: A feasibility study," *IEEE Trans. Intell. Trans. Syst.*, vol. 16, no. 4, pp. 1784–1793, Jan. 2015.

[6] D. W. Matolak and Q. Wu, "Channel models for V2V communications: A comparison of different approaches," in *Proc. EUCAP*, Rome, Italy, Apr. 2011, pp. 2891–2895.

[7] A. F. Molisch, F. Tufvesson, J. Kåredal, and C. F. Mecklenbräuker, "A survey on vehicle-to-vehicle propagation channels," *IEEE Commun. Mag.*, vol. 16, no. 6, pp. 12–22, Dec. 2009.

[8] S. Wu, C.-X. Wang, M. Aggoune, M. M. Alwakeel, and X. H. You, "A general 3-D non-stationary 5G wireless channel model," *IEEE Trans. Commun.*, vol. 66, no. 7, pp. 3065–3078, Jul. 2018.

[9] M. Herdin, N. Czink, H. Ozcelik, and E. Bonek, "Correlation matrix distance, a meaningful measure for evaluation of non-stationary MIMO channels," in *Proc. IEEE VTC-Spring*, vol. 1, Stockholm, Sweden, May 2005, pp. 136–140.

[10] L. Bernadó, T. Zemen, F. Tufvesson, A. F. Molisch, and C. F. Mecklenbräuker, "Delay and Doppler spreads of nonstationary vehicular channels for safety-relevant scenarios," *IEEE Trans. Veh. Technol.*, vol. 63, no. 1, pp. 82–93, Jan. 2014.

[11] X. Cheng, C.-X. Wang, D. I. Laurenson, S. Salous, and A. V. Vasilakos, "An adaptive geometry-based stochastic model for non-isotropic MIMO mobile-to-mobile channels," *IEEE Trans. Wireless Commun.*, vol. 8, no. 9, pp. 4824–4835, Sep. 2009.

[12] X. Cheng, C.-X. Wang, B. Ai, and H. Aggoune, "Envelope level crossing rate and average fade duration of nonisotropic vehicle-to-vehicle Ricean fading channels," *IEEE Trans. Intell. Transp. Syst.*, vol. 15, no. 1, pp. 62–72, Feb. 2014.

[13] A. G. Zajić and G. L. Stuber, "Three-dimensional modeling and simulation of wideband MIMO mobile-to-mobile channels," *IEEE Trans. Wireless Commun.*, vol. 8, no. 3, pp. 1260–1275, Mar. 2009.

[14] A. G. Zajić, G. L. Stuber, T. G. Pratt, and S. T. Nguyen, "Wideband MIMO mobile-to-mobile channels: Geometry-based statistical modeling with experimental verification," *IEEE Trans. Veh. Technol.*, vol. 58, no. 2, pp. 517–534, Feb. 2009.

[15] Y. Yuan, C.-X. Wang, X. Cheng, B. Ai, and D. I. Laurenson, "Novel 3D geometry-based stochastic models for non-isotropic MIMO vehicle-to-vehicle channels," *IEEE Trans. Wireless Commun.*, vol. 13, no. 1, pp. 298–309, Jan. 2014.

[16] L. Bernadó, T. Zemen, F. Tufvesson, A. F. Molisch, and C. F. Mecklenbräuker, "The (in-) validity of the WSSUS assumption in vehicular radio channels," in *Proc. IEEE PIMRC*, Sydney, NSW, Australia, Sep. 2012, pp. 1757–1762.

[17] J. Bian *et al.*, "A WINNER+ based 3-D non-stationary wideband MIMO channel model," *IEEE Trans. Wireless Commun.*, vol. 17, no. 3, pp. 1755–1767, Mar. 2018.

[18] A. Chelli and M. Pätzold, "A non-stationary MIMO vehicle-to-vehicle channel model derived from the geometrical street model," in *Proc. IEEE VTC-Fall*, San Francisco, CA, USA, Sep. 2011, pp. 1–6.

[19] A. Chelli and M. Pätzold, "A non-stationary MIMO vehicle-to-vehicle channel model based on the geometrical T-junction model," in *Proc. WCSP*, Nanjing, China, Nov. 2009, pp. 1–5.

[20] Y. Yuan, C.-X. Wang, Y. He, M. M. Alwakeel, and E.-H. M. Aggoune, "3D wideband non-stationary geometry-based stochastic models for non-isotropic MIMO vehicle-to-vehicle channels," *IEEE Trans. Wireless Commun.*, vol. 14, no. 12, pp. 6883–6895, Dec. 2015.

[21] A. Borhani and M. Pätzold, "Correlation and spectral properties of vehicle-to-vehicle channels in the presence of moving scatterers," *IEEE Trans. Veh. Technol.*, vol. 62, no. 9, pp. 4228–4239, Nov. 2013.

[22] I. Sen and D. W. Matolak, "Vehicle–vehicle channel models for the 5-GHz band," *IEEE Trans. Intell. Transp. Syst.*, vol. 9, no. 2, pp. 235–245, Jun. 2008.

[23] D. W. Matolak, "Channel modeling for vehicle-to-vehicle communications," *IEEE Commun. Mag.*, vol. 46, no. 5, pp. 76–83, May 2008.

[24] R. He *et al.*, "A dynamic wideband directional channel model for vehicle-to-vehicle communications," *IEEE Trans. Ind. Electron.*, vol. 62, no. 12, pp. 7870–7882, Dec. 2015.

[25] M. Pätzold and C. A. Gutierrez, "The Wigner distribution of sum-of-cissoids and sum-of-chirps processes for the modelling of stationary and non-stationary mobile channels," in *Proc. IEEE VTC-Spring*, Nanjing, China, May 2016, pp. 1–5.

[26] W. Dahech and M. Pätzold, C. A. Gutiérrez, and N. Youssef, "A non-stationary mobile-to-mobile channel model allowing for velocity and trajectory variations of the mobile stations," *IEEE Trans. Wireless Commun.*, vol. 16, no. 3, pp. 1987–2000, Mar. 2017.

[27] C. A. Gutierrez and M. Pätzold, W. Dahech, and N. Youssef, "A non-WSSUS mobile-to-mobile channel model assuming velocity variations of the mobile stations," in *Proc. IEEE WCNC*, San Francisco, CA, USA, Mar. 2017, pp. 1–6.

[28] J. Bian, C.-X. Wang, M. Zhang, X. Ge, and X. Gao, "A 3-D Non-stationary wideband MIMO channel model allowing for velocity variations of the mobile station," in *Proc. IEEE ICC*, Paris, France, May 2017, pp. 1–6.

[29] R. He, B. Ai, G. L. Stüber, and Z. Zhong, "Mobility model-based non-stationary mobile-to-mobile channel modeling," *IEEE Trans. Wireless Commun.*, vol. 17, no. 7, pp. 4388–4400, Jul. 2018.

[30] Q. Zhu *et al.*, "A novel 3D non-stationary vehicle-to-vehicle channel model and its spatial-temporal correlation properties," *IEEE Access*, vol. 6, pp. 43633–43643, 2018.

[31] J. Meinila *et al.*, *WINNER+ Final Channel Models*, document CELTIC/CP5-026 D5.3, Jun. 2010.

[32] P. Kyösti *et al.*, *WINNER II Channel Models*, document IST-4-027756, WINNER II D1.1.2, v1.2, Apr. 2008.

[33] Q. Zhu *et al.*, "A novel 3D non-stationary wireless MIMO channel simulator and hardware emulator," *IEEE Trans. Commun.*, vol. 66, no. 9, pp. 3865–3878, Sep. 2018.

[34] R. Verdone and A. Zanella, *Pervasive Mobile and Ambient Wireless Communications*. London, U.K.: Springer, 2012.

[35] A. Ghazal *et al.*, "A non-stationary IMT-advanced MIMO channel model for high-mobility wireless communication systems," *IEEE Trans. Wireless Commun.*, vol. 16, no. 4, pp. 2057–2068, Apr. 2017.

[36] M. Ozcelik, N. Czink, and E. Bonek, "What makes a good MIMO channel model?" in *Proc. IEEE VTC*, vol. 1, May/Jun. 2005, pp. 156–160.

[37] T. Betlehem, T. A. Lamahewa, and T. D. Abhayapala, "Dependence of MIMO system performance on the joint properties of angular power," in *Proc. IEEE ISIT*, Seattle, WA, USA, Jul. 2006, pp. 2849–2853.

[38] M. Pätzold and C. A. Gutierrez, "Modelling and analysis of non-stationary multipath fading channels with time-variant angles of arrival," in *Proc. IEEE VTC-Spring*, Sydney, NSW, Australia, Jun. 2017, pp. 1–6.

[39] A. G. Zajić and G. L. Stüber, "Space-time correlated mobile-to-mobile channels: Modelling and simulation," *IEEE Trans. Veh. Technol.*, vol. 57, no. 2, pp. 715–726, Mar. 2008.

[40] K. Mammasis, E. Pfann, R. W. Stewart, and G. Freeland, "Three-dimensional channel modelling using spherical statistics for smart antennas," *Electron. Lett.*, vol. 44, no. 2, pp. 136–137, Jan. 2008.

[41] Y. Liu, C.-X. Wang, C. Lopez, and X. Ge, "3D non-stationary wideband circular tunnel channel models for high-speed train wireless communication systems," *Sci. China Inf. Sci.*, vol. 60, no. 8, pp. 189–201, Aug. 2017. doi: 10.1007/s11432-016-9004-4.

[42] I. S. Gradshteyn and I. M. Ryzhik, *Table of Integrals, Series, and Products*, 7th ed. Boston, MA, USA: Academic, 2007.

[43] B. Boashash, G. Jones, and P. O'Shea, "Instantaneous frequency of signals: Concepts, estimation techniques and applications," *Proc. SPIE*, vol. 1152, pp. 382–401, Nov. 1989.

[44] C. X. Wang, A. Ghazal, B. Ai, P. Fan, and Y. Liu, "Channel measurements and models for high-speed train communication systems: A survey," *IEEE Commun. Surveys Tuts.*, vol. 18, no. 2, pp. 974–987, 2nd Quart., 2016.

[45] A. Gehring, M. Steinbauer, I. Gaspard, and M. Grigat, "Empirical channel stationarity in urban environments," in *Proc. EPMCC*, Vienna, Austria, Feb. 2001.

[46] T. T. Georgiou, "Distances and Riemannian metrics for spectral density functions," *IEEE Trans. Signal Process.*, vol. 55, no. 8, pp. 3995–4003, Aug. 2007.
[47] M. Pätzold and C. A. Gutierrez, "Definition and analysis of quasi-stationary intervals of mobile radio channels-invited paper," in *Proc. IEEE VTC-Spring*, Porto, Portugal, Jun. 2018, pp. 1–6.
[48] J. Maurer, T. Fugen, and W. Wiesbeck, "Narrow-band measurement and analysis of the inter-vehicle transmission channel at 5.2 GHz," in *Proc. IEEE VTC-Spring*, Birmingham, AL, USA, May 2002, pp. 1274–1278.
[49] L. Cheng, B. E. Henty, D. D. Stancil, F. Bai, and P. Mudalige, "Mobile vehicle-to-vehicle narrow-band channel measurement and characterization of the 5.9 GHz dedicated short range communication (DSRC) frequency band," *IEEE J. Sel. Areas Commun.*, vol. 25, no. 8, pp. 1501–1516, Oct. 2007.

JI BIAN received the B.Sc. degree in electronic information science and technology from Shandong Normal University, Jinan, China, in 2010, and the M.Sc. degree in signal and information processing from the Nanjing University of Posts and Telecommunications, Nanjing, China, in 2013. He is currently pursuing the Ph.D. degree with the School of Information Science and Engineering, Shandong University, Qingdao, China.

He was an Academic Visitor with Heriot-Watt University, U.K., from 2017 to 2018. His current research interests include channel measurements, wireless propagation channel characterization, and 5G channel modeling.

CHENG-XIANG WANG (S'01–M'05–SM'08–F'17) received the B.Sc. and M.Eng. degrees in communication and information systems from Shandong University, China, in 1997 and 2000, respectively, and the Ph.D. degree in wireless communications from Aalborg University, Denmark, in 2004.

He was a Research Assistant with the Hamburg University of Technology, Hamburg, Germany, from 2000 to 2001, a Visiting Researcher with Siemens AG Mobile Phones, Munich, Germany, in 2004, and a Research Fellow with the University of Agder, Grimstad, Norway, from 2001 to 2005. He has been with Heriot-Watt University, Edinburgh, U.K., since 2005, where he was promoted to a Professor in 2011. In 2018, he joined Southeast University, China, as a Professor. He has authored three books, one book chapter, and more than 350 papers in refereed journals and conference proceedings, including 23 Highly Cited Papers. He has also delivered 17 Invited Keynote Speeches/Talks and six Tutorials in international conferences. His current research interests include wireless channel measurements and modeling, (B)5G wireless communication networks, and applying artificial intelligence to wireless communication networks.

Dr. Wang is a Fellow of the IET, an IEEE Communications Society Distinguished Lecturer in 2019 and 2020, and a Highly-Cited Researcher recognized by Clarivate Analytics in 2017 and 2018. He received nine Best Paper Awards from IEEE GLOBECOM 2010, IEEE ICCT 2011, ITST 2012, IEEE VTC 2013-Spring, IWCMC 2015, IWCMC 2016, IEEE/CIC ICCC 2016, and WPMC 2016. He has served as an Editor for nine international journals, including the IEEE TRANSACTIONS ON WIRELESS COMMUNICATIONS from 2007 to 2009, the IEEE TRANSACTIONS ON VEHICULAR TECHNOLOGY from 2011 to 2017, and the IEEE TRANSACTIONS ON COMMUNICATIONS from 2015 to 2017. He was a Guest Editor for the IEEE JOURNAL ON SELECTED AREAS IN COMMUNICATIONS, Special Issue on Vehicular Communications and Networks (Lead Guest Editor), Special Issue on Spectrum and Energy Efficient Design of Wireless Communication Networks, and Special Issue on Airborne Communication Networks. He was also a Guest Editor for the IEEE TRANSACTIONS ON BIG DATA, Special Issue on Wireless Big Data. He has served as a TPC Member, a TPC Chair, and a General Chair for more than 80 international conferences.

JIE HUANG received the B.Sc. degree in information engineering from Xidian University, China, in 2013, and the Ph.D. degree in communication and information systems from Shandong University, China, in 2018. Since 2018, he has been a Postdoctoral Research Associate with the Mobile Communications Research Laboratory, Southeast University, China. In 2019, he was an Academic Visitor with the Durham University, U.K. His current research interests include millimeter wave and massive MIMO channel measurements, parameter estimation, channel modeling, wireless big data, and 5G wireless communications.

YU LIU received the B.Sc. and M.Eng. degrees in communication and information systems from Qufu Normal University, China, in 2010 and 2013, respectively, and the Ph.D. degree in communication and information systems from Shandong University, China, in 2017. Since 2017, she has been holding a postdoctoral position with the School of Information Science and Engineering, Shandong University, China. Her current research interests include non-stationary channel modeling, high-speed train wireless propagation characterization and modeling, and channel modeling for special scenarios.

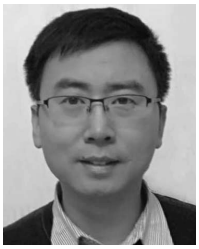

JIAN SUN (M'08) received the B.Sc. degree in applied electronic technology, the M.Eng. degree in measuring and testing technologies and instruments, and the Ph.D. degree in communication and information systems from Zhejiang University, Hangzhou, China, in 1996, 1999, and 2005, respectively.

Since 2005, he has been a Lecturer with the School of Information Science and Engineering, Shandong University, China. In 2011, he was a Visiting Scholar with Heriot-Watt University, U.K., supported by U.K.–China Science Bridges: R&D on (B)4G Wireless Mobile Communications project. His current research interests include signal processing for wireless communications, channel sounding and modeling, propagation measurement and parameter extraction, MIMO, and multicarrier transmission systems design and implementation.

MINGGAO ZHANG received the B.Sc. degree in mathematics from Wuhan University, China, in 1962.

He is currently a Distinguished Professor with the School of Information Science and Engineering, Shandong University, the Director of Academic Committee of China Rainbow Project Collaborative Innovation Center, the Director of Academic Committee of Shandong Provincial Key Lab of Wireless Communication Technologies, and a Senior Engineer of the No. 22 Research Institute of China Electronics Technology Corporation. He has been an Academician of Chinese Academy of Engineering since 1999, where he is currently a Fellow of the China Institute of Communications. He was a Group Leader of the Radio Transmission Research Group, ITU-R.

He has been engaged in the research of radio propagation for decades. Many of his proposals have been adopted by international standardization organizations, including CCIR P.617-1, ITU-R P.680-3, ITU-R P.531-5, ITU-R P.529-2, and ITU-R P.676-3. In addition, he has received seven national and ministerial-level Science and Technology Progress Awards in China.

EL-HADI M. AGGOUNE (M'83–SM'93) received the M.S. and Ph.D. degrees in electrical engineering from the University of Washington (UW), Seattle, WA, USA. He taught graduate and undergraduate courses in electrical engineering at many universities in the USA and abroad. He served at many academic ranks, including an Endowed Chair Professor. He is listed as an Inventor in two patents assigned to the Boeing Company, USA, and the Sensor Networks and Cellular Systems Research Center, University of Tabuk, Saudi Arabia. He is a Professional Engineer registered in the State of Washington. He is currently serving as a Professor and the Director of the SNCS Research Center, University of Tabuk. His research is referred to in many patents, including patents assigned to ABB, Switzerland, and EPRI, USA. He authored many papers in IEEE and other journals and conferences. His research interests include wireless sensor networks, energy systems, and scientific visualization. He is serving on many technical committees for conferences worldwide and reviewer for many journals. One of his Laboratories received the Boeing Supplier Excellence Award. He also received the IEEE Professor of the Year Award, UW Branch.